Bulletin of Mathematical Biology (2003) **65**, 693–730
doi:10.1016/S0092-8240(03)00030-2

Chemotactic Signaling, Microglia, and Alzheimer's Disease Senile Plaques: Is There a Connection?

MAGDALENA LUCA[*][†]
Massachusetts College of Pharmacy and Health Sciences,
School of Arts and Sciences,
179 Longwood Avenue,
Boston, MA 02115-5896,
U.S.A.
E-mail: magdalena.luca@mcp.edu

ALEXANDRA CHAVEZ-ROSS[‡] AND LEAH EDELSTEIN-KESHET
Room 1211984, Mathematics Road,
Mathematics Annex 1111,
Department of Mathematics,
University of British Columbia,
Vancouver, British Columbia,
Canada V6T 1Z2
E-mail: alex@pims.math.ca, keshet@math.ubc.ca

ALEX MOGILNER
Department of Mathematics and Center for Genetics and Development,
University of California, Davis,
One Shields Avenue,
Davis, CA 95616,
U.S.A.
E-mail: mogilner@math.ucdavis.edu

Chemotactic cells known as microglia are involved in the inflammation associated with pathology in Alzheimer's disease (AD). We investigate conditions that lead to aggregation of microglia and formation of local accumulations of chemicals observed in AD senile plaques. We develop a model for chemotaxis in response to a combination of chemoattractant and chemorepellent signaling chemicals. Linear stability analysis and numerical simulations of the model predict that periodic patterns in cell and chemical distributions can evolve under local attraction, long-ranged repulsion, and other constraints on concentrations and diffusion coefficients of the chemotactic signals. Using biological parameters from the literature, we compare and discuss the applicability of this model to actual processes in AD.

---

[*] Author to whom correspondence should be addressed.

[†] Reprint address.

[‡] Maternity leave.

1. INTRODUCTION

This paper presents an investigation into chemotaxis systems in which motile cells induce the production of a number of diffusible signaling chemicals whose distribution influences motion of the cells. A novel aspect of the model is that it includes both chemoattraction and chemorepulsion. We show how the magnitudes and spatial ranges of the chemical signals combine to cause instability of a homogeneous distribution, and to determine spacing of the cell and chemical aggregates.

The investigation was motivated by phenomena associated with formation of senile plaques, abnormal foci that form in the central nervous system (CNS) in Alzheimer's disease (AD), though the chemicals we discuss cannot be definitively identified given current biological knowledge. However, information about the possible ranges of parameter values associated with the disease have been extracted from the literature, to be used as a testing arena for what is essentially an abstract theory.

We briefly describe some aspects of the disease in the next section. We review earlier chemotaxis modeling work in Section 3, introduce the model in Sections 4 and 5, and perform linear stability analysis in Sections 6 and 7. In Section 8, we estimate parameter values (see also details in the appendix). This is followed, in Sections 9 and 10 by a description of the adaptive mesh numerical method used for integrating the equations and numerical results. A generalization of the pattern formation is described in Section 11. The biomedical implications of the model, limitations and open questions are discussed in Section 12.

2. BIOLOGICAL BACKGROUND OF ALZHEIMER'S DISEASE

AD is a devastating neurodegenerative disease affecting almost one out of 10 individuals above the age of 60, and more than half of those reaching age 85 (Cowley, 2000; Jones, 2000). The disease represents the eighth leading cause of death in America, and has a typical duration of 8–20 years (Nash, 2000). AD is characterized by a progressive decline of cognitive and mental function, and eventual death. Although the details in the pathology and the underlying causes of the disease are still controversial, a number of leading hypotheses have been put forward in recent years.

It is now well established that the brains of AD sufferers develop abnormal foci called **senile plaques** (Itagaki *et al.*, 1989; Dickson, 1997), i.e., lesions composed of extracellular deposits of the β**-amyloid protein**, degenerating neurons and other nonneuronal cells called **glia** (Dickson, 1997). **Amyloid plaques** are the major biological markers of AD. They range in size from approximately 10 to 100 μm, and their distance apart is about 50–200 μm. Postmortem preparations reveal 30 amyloid plaques per 10^4 μm^2 of affected regions in the AD brain (Itagaki *et al.*, 1989).

According to the *amyloid cascade hypothesis*, initial stages of AD include local accumulation of **soluble** β**-amyloid protein** [high levels correlate with the severity of the disease (McLean *et al.*, 1999)]. This leads to local deposits called **diffuse plaques** (Banati and Beyreuther, 1995) that, over time, build up to form relatively insoluble **dense plaques** (Banati and Beyreuther, 1995). Some researchers (Selkoe, 1991; Davis and Chisholm, 1997; Hardy, 1997) believe that this is the main cause of the pathology and the resultant stress and death of neurons in the central nervous system (Kowall, 1994; Sheng *et al.*, 1998). AD is associated with an inflammation involving cells called microglia and astrocytes. Following activation, these glial (nonneuronal) cells proliferate, and migrate chemotactically to sites of injury, where they secrete a host of chemicals, including cytokines.

We will mainly be concerned here with the role of microglia, early in the development of diffuse senile plaques, though astrocytes are also implicated in later stages. **Microglia** are 10–15 μm in size (Streit, 1995), distributed sparsely in the brains of healthy individuals [e.g., 0.3 cells per 10^4 μm^2 in temporal neocortex (Mackenzie *et al.*, 1995)], but found at much higher densities in AD: Itagaki *et al.* (1989) observed between 100 and 350 reactive microglia cells in a section 10^4 μm^2 in area and 30 μm thick in a hippocampus of an Alzheimer's patient (Fig. 5 of their paper). This high density is believed to result from aggregation, rather than proliferation of the cells (P. McGeer, personal communication).

Microglia move chemotactically with an estimated speed of 1–2 $\mu\text{m min}^{-1}$ (Farrell *et al.*, 1990), in response to concentration gradients of amyloid proteins and other factors (Itagaki *et al.*, 1989). The chemotactic sensitivity of microglia to amyloid proteins (Davis *et al.*, 1992), to various cytokines and proteins (Yao *et al.*, 1990; Chicoine *et al.*, 1995), and the general motility of these cells (Nolte *et al.*, 1996) has been studied extensively.

Glial cells produce cytokines and other inflammatory factors (Mrak *et al.*, 1995, 2000) with positive feedback via neuronal stress. Among the major cytokines implicated in AD, **Interleukin-1** (IL-1; molecular weight 17 kDa) is produced by microglia (Benveniste, 1995), and induces production of other cytokines, such as IL-6, TNF-α by astrocytes and other cells (Nilsson *et al.*, 1998). Further, IL-1 induces astrocytes and neurons to produce more β-amyloid which leads to deposition of amyloid fibrils (Nilsson *et al.*, 1998). **Interleukin-6** (IL-6; 26 kDa) is secreted mainly by astrocytes (Benveniste, 1995) stimulated by IL-1β (Lee *et al.*, 1993). Elevated levels of IL-6 are observed when senile plaques start to form (Nilsson *et al.*, 1998). **Tumor necrosis factor-α** (TNF-α; 17 kDa) is mainly secreted by stimulated astrocytes and is believed to trigger apoptosis (programmed cell death), in some types of cells, and may act as a chemorepellent under some conditions (Chicoine *et al.*, 1995; Venters *et al.*, 2000).

3. REVIEW OF CHEMOTAXIS MODELS

Keller and Segel developed the first mathematical model for interactions of chemotactic cells (slime molds) and a secreted attractant (cAMP), and showed that the onset of cell aggregation can be regarded as an instability (Keller and Segel, 1970). A typical formulation for the system of equations for chemotaxis models in the form of a coordinate-free system is:

$$
\begin{aligned}
\frac{\partial m}{\partial t} &= \nabla \cdot (\mu \nabla m) - \nabla \cdot (\chi m \nabla c) + f(m, c), \\
\frac{\partial c}{\partial t} &= \nabla \cdot (D \nabla c) + g(m, c),
\end{aligned} \tag{1}
$$

where m is the cell density, and c is the chemoattractant concentration. $\mu > 0$ and χ are the cell motility and chemotactic coefficient, respectively. The sign of χ corresponds to chemoattraction if positive, and repulsion if negative. $D > 0$ is the diffusion coefficient of the chemical and $g(m, c)$ represents production and/or degradation of chemicals. Cell proliferation and death is depicted by $f(m, c)$. Examples of specific variants of the system (1) are shown in Table 1. Unless otherwise stated, these models have been studied in one-dimensional space with Neumann (no-flux) boundary conditions.

Three forms of the concentration-dependent chemotactic coefficient, $\chi(c)$, were discussed by Schaaf (1985): (1) $\chi(c) = \chi =$ constant, (2) $\chi(c) = 1/c$, and (3) a receptor-kinetics form $\chi(c) = 1/(k + c)^2$, where $k > 0$. Concentration-dependence of the random motility term, $\mu(c)$, was discussed by Rivero (Rivero *et al*., 1989). The rate of removal of chemicals is linear in some models, but when binding of chemicals to cell-surface receptors is considered, removal rates of the form $g(m, c) \propto mc/(k + c)$ are used.

Experimental observations of individual cells, and arguments based on theoretical considerations have been used to develop population-level models from underlying stochastic mechanisms and to estimate parameters for the random motility coefficient and the chemotaxis coefficient (Tranquillo *et al*., 1988; Rivero *et al*., 1989; Sherratt *et al*., 1992). It is necessary to connect the details of the motion of the individual with that of the group. Papers that have addressed this problem, and derived the appropriate partial or integro-partial differential equations include (Alt, 1980; Othmer *et al*., 1988) and, in an ecological setting, (Grunbaum, 1994, 1999). Othmer and Stevens (1997) modeled *myxobacteria*, as individual random walkers. They derived a master equation for the bacterial probability density as a continuous-time discrete-space random walk, and used this to develop the continuous time and space equation.

3.1. ***Analytical techniques in chemotaxis models.*** Several common forms of analyses, including linear stability analysis, have been applied to chemotaxis to model established conditions leading to instability of homogeneous steady states. Grindrod *et al*. (1989) analyzed the local and global bifurcation of spatially heterogeneous patterns away from the homogeneous steady states as the number of cells increased. They also discussed periodic spatially distributed solutions for the cells and attractant in an infinite domain.

Table 1. A summary of assumed forms for cell birth/death, $f(m, c)$, and chemical production/decay rates, $g(m, c)$, in chemotaxis models of the general form shown in equation (1).

Source	$f(m,c)$	$g(m,c)$	Comments
Grindrod *et al.* (1989)	0	$b\dfrac{m}{m+h} - \mu c$	Existence and stability of solutions
Maini *et al.* (1991)	$srm(N-m)$	$s\left(\dfrac{m}{m+1} - c\right)$	Domain effects on dynamics
Myerscough *et al.* (1998)	$srm(1-m)$	$s\left(\dfrac{m}{m+\gamma} - c\right)$	Boundary effects on dynamics
Lauffenburger and Kennedy (1983)	$\alpha(1-\sigma c-m)$	$\dfrac{\gamma c}{1+c} - \dfrac{mc}{k+c}$	Applications to white blood cells and bacteria
Sherratt (1994)	0	$-\delta(c)m$	$D \equiv D(c)$ $\chi \equiv \chi(c)$ applications to eukaryotic cells
Othmer and Stevens (1997)	0	$\dfrac{mc}{1+\nu c} - \mu c + \gamma_r \dfrac{m}{1+m}$	$\chi \equiv \chi(c)$, $D = 0$ applications to *myxobacteria*
Painter *et al.* (1999)	0	$g_1(c_1, c_2) - (r_1 + r_2)c_1$ $g_2(c_1, c_2) - (r_1 + r_2)c_2$	One cell type, two chemicals. 2D, $\chi \equiv \chi(c_1)$
Painter *et al.* (2000)	0	$g_1(c_1, c_2)$, $g_2(c_1, c_2)$	One cell type, two chemicals. 2D, $\chi \equiv \chi(c_1, c_2)$

A two-dimensional chemotaxis model was investigated analytically and numerically by Maini *et al.* (1991) with logistic growth for the cells and a Michaelis-Menten production rate of attractant. The authors investigated the roles of symmetric and asymmetric mixed boundary conditions, domain size, and aspect ratio on the formation of stripes and spots. They noted that when the total number of cells were increased, the number of aggregates also increased.

Othmer and Stevens (1997) studied finite time blow-up solutions, representing strong aggregation in *myxobacteria*. In a series of numerical examples, they demonstrated interplay between chemotactic sensitivity, the rate of production of the chemical and initial conditions. Some solutions collapsed to a uniform steady state, while others formed high amplitude peaks, or a sequence of decreasing plateaus. The authors showed that stable aggregation can occur in the absence of long-range signaling. A one-dimensional hyperbolic model for chemotaxis has been analyzed by Hillen and Stevens (2000). Both globally stable patterns and blow-up solutions were found.

A paper by Lee *et al.* (2001) places chemotaxis in the context of local and nonlocal mathematical models for biological phenomena. The authors constructed a one-dimensional model for chemotaxis of myxobacteria, similar to the Keller–Segel model and showed the connection to a formulation in which long-range signaling occurs between cells.

3.2. *Biological applications.* Chemotaxis models have been applied to inflammatory response of cells in the immune system, including polymorphonuclear leukocytes (PMN) (Lauffenburger and Kennedy, 1983; Tranquillo *et al.*, 1988; Rivero *et al.*, 1989). In these models, aggregates represent localized regions of inflammation and foci of infection. In contrast with the interactions in the Keller–Segel model, the role of cells is to remove, rather than produce the attractant.

Several chemotaxis models have been applied to formation of patterns on animal skin (Maini *et al.*, 1991; Myerscough *et al.*, 1998). A generalized Turing model with chemotaxis was developed by Painter *et al.* (1999) to account for cell growth and movement. The authors analyzed the effects of these two processes on pigment patterning in a system of stripes on a growing angelfish *Pomacanthus*. In addition, chemotaxis in response to chemical gradients (of one of the two chemicals) led to aggregation of one type of pigment cell into a striped spatial pattern. The chemotactic substance was taken to be a chemorepellent, with concentration-dependent chemotactic coefficient, $\chi(c) = \chi_0/(k^2 + c^2)$ and $\chi_0 < 0$. (The other chemical influenced the production of this repellent.) The system of three equations was shown to lead to stripes that split into finer stripes as the domain size increased.

Most of the original chemotactic models considered interactions between one cell type and one chemical. However, an attractant and a repellent were considered by Painter *et al.* (2000) in a generalization of Othmer and Stevens (1997). Numerical simulations for a one-dimensional and a two-dimensional model revealed the formation of patterns such as spots and stripes of various thickness, representative of spots on a jaguar and stripes on a lion-fish.

4. MODELING GOALS

Our purpose in this paper is to investigate whether some generic aspects of plaque distribution, such as spacing (or density) might be correlated with the level of reactive microglia and their known chemotactic behavior. Here we leave out many important aspects of AD. In a separate paper (Edelstein-Keshet and Spiros, 2002), we included further biological details of the inflammation and death of neurons, and the involvement of microglia, astrocytes, and several secreted cytokines.

In principle, the actual sites at which senile plaques form in AD might have a purely stochastic determinant: perhaps injury, excitotoxic factors, or oxidative stress cause a few neurons here or there to defectively process precursor proteins into β-amyloid, initiating foci destined to become plaques. In this case, one would ask what subcellular events lead to such stress and abnormal neuronal behavior, rather than how interactions of a population of glial cells determines the development of plaques. If so, then, our model has little relevance.

Another possibility, motivating our own investigation, is that global inflammation in the brain leads to an elevation in reactive microglia, that, interacting through their own signaling chemicals, spontaneously aggregate, forming the foci for senile plaques. While there is no definitive evidence that would, at present, confirm or rule out this possibility, we can formulate this as a hypothesis to test. With the availability of some biological parameter values governing typical rates of diffusion, chemotaxis, and chemical production/decay in the brain, we then compare predictions of such a model to observed plaque spacing. We thus ask: what types of interactions between microglia and their secreted chemical factors would lead to the formation of localized aggregates representative of diffuse senile plaques? Is such behavior possible within biologically relevant parameter regimes?

5. DERIVATION OF THE MODEL

With the multiplicity of chemical factors and cytokines known to occur in immune-like signaling cascades, we were interested in assessing how some combination of chemicals, e.g., those that lead to repulsion and/or attraction of the responding cells might interact to produce aggregates. In the CNS, and particularly so during development, this type of interaction has a documented basis: chemorepulsion and chemoattraction of netrins and semaphorins are well known (Mark *et al*., 1997; de Castro *et al*., 1999; Bagnard *et al*., 2000). The cytokines IL-1β and IL-6, implicated in AD, are either secreted by microglia, or secreted by other cells in response to microglial signaling (Lee *et al*., 1993; Mackenzie *et al*., 1995; Stalder *et al*., 1999; Mrak *et al*., 2000; Smits *et al*., 2000), and are known to affect the motion of microglia. Some are known to be attractants (e.g., β-amyloid, IL-1 proteins) and circumstantial evidence suggests a chemorepellent role for TNF-α (Chicoine *et al*., 1995) under certain conditions.

5.1. ***Chemoattraction–repulsion model equations.*** For simplicity, we take a one-dimensional domain, $0 < x < L$, where L is a typical dimension of a relevant domain in the brain. We consider cell density, m, representing activated microglia and c_i, chemical concentrations of attractant ($i = 1$) and repellent ($i = 2$). We assume that microglia undergo random motion (motility coefficient $\mu =$ constant) and chemotaxis towards attractant (chemotactic coefficient $\chi_1 =$ constant) and away from repellent (chemotactic coefficient $\chi_2 =$ constant). No proliferation or death of cells is considered. We assume that chemicals diffuse in the region with constant diffusion coefficients D_i. With these assumptions, the model equations are:

$$\frac{\partial m}{\partial t} = \mu \frac{\partial^2 m}{\partial x^2} - \frac{\partial}{\partial x}\left(\chi_1 m \frac{\partial c_1}{\partial x} - \chi_2 m \frac{\partial c_2}{\partial x}\right), \tag{2}$$

$$\frac{\partial c_i}{\partial t} = D_i \frac{\partial^2 c_i}{\partial x^2} + a_i m - b_i c_i \qquad i = 1, 2. \tag{3}$$

Here a_i, b_i's are rates of production and decay of the chemicals, respectively. The decay of chemicals follows simple linear kinetics, representing uptake by surrounding tissue, or deactivation by some other mechanism. The production of chemicals is taken to be proportional to the density of chemotactic cells. This represents either a constant rate of secretion by the cells, or indirect production by other cell types in response to local effects of the motile cells. For example, microglial IL-1β enhances the processing and production of amyloid by neuronal tissue. Equation (2) does not include a term for proliferation, held to be insignificant for microglia in adult brain (P. McGeer, personal communication).

We consider no-flux boundary conditions:

$$\mu \frac{\partial m}{\partial x} - \left(\chi_1 m \frac{\partial c_1}{\partial x} - \chi_2 m \frac{\partial c_2}{\partial x}\right) = 0, \tag{4}$$

$$\left.\frac{\partial c_i}{\partial x}\right|_{x=0,L} = 0. \tag{5}$$

(Preliminary numerical experiments establish that these boundary conditions do not significantly affect the solutions qualitatively.)

To recast the model in a dimensionless form, choose the constant average cell density, $\bar{m}$, as the scale for microglia density. The average concentration of the chemicals at which production and decay balance, $(a_i \bar{m}/b_i)$, form characteristic scales for chemical concentrations. The effective spatial ranges for the attractant (L_1) and repellent (L_2), are $L_i = \sqrt{D_i/b_i}$, $i = 1, 2$, i.e., the distance over which chemicals spread during the characteristic time of decay. We take L_2 as the characteristic length scale of the problem. Then the time needed for a cell to move over one unit of this length scale, $\tau = L_2^2/\mu$, can be used as a time scale. Introducing the dimensionless variables:

$$x^* = \frac{x}{\hat{x}}, \qquad t^* = \frac{t}{\hat{t}}, \qquad m^* = \frac{m}{\hat{m}}, \qquad c_i^* = \frac{c_i}{\hat{c}_i},$$

where the scales are:

$$\hat{m} = \bar{m}, \qquad \hat{c}_i = a_i \bar{m}/b_i, \qquad i = 1, 2,$$
$$\hat{x} = L_2 = \sqrt{D_2/b_2}, \qquad \hat{t} = \tau = L_2^2/\mu, \tag{6}$$

we obtain the following nondimensional system of equations, where the stars have been dropped for notational convenience:

$$\frac{\partial m}{\partial t} = \frac{\partial^2 m}{\partial x^2} - \frac{\partial}{\partial x}\left[\left(A_1\frac{\partial c_1}{\partial x} - A_2\frac{\partial c_2}{\partial x}\right)m\right], \tag{7}$$

$$\epsilon_1\frac{\partial c_1}{\partial t} = \frac{\partial^2 c_1}{\partial x^2} + a^2(m - c_1), \tag{8}$$

$$\epsilon_2\frac{\partial c_2}{\partial t} = \frac{\partial^2 c_2}{\partial x^2} + m - c_2. \tag{9}$$

The model behavior is characterized by five dimensionless parameters:

$$A_1 = \frac{\chi_1 a_1 \bar{m}}{\mu b_1}, \qquad A_2 = \frac{\chi_2 a_2 \bar{m}}{\mu b_2}, \qquad \epsilon_1 = \frac{\mu}{D_1},$$
$$\epsilon_2 = \frac{\mu}{D_2}, \qquad a = \frac{L_2}{L_1}. \tag{10}$$

We also define the ratio

$$A = \frac{\chi_1}{\chi_2}\frac{a_1}{a_2}\frac{D_2}{D_1} \tag{11}$$

which appears in a later discussion. A represents the ratio of effective strengths of the attraction and repulsion, while a represents the ratio of the spatial ranges of the repulsion and attraction.

5.2. ***Relation to nonlocal signaling model.*** The connection between chemical signaling and nonlocal interaction models has been investigated by Lee *et al.* (2001). They demonstrated that when chemicals diffuse much more rapidly than cells, i.e., $\mu \ll D_i$, (which implies $\epsilon_i \ll 1$), a **quasi-stationary** distribution of chemicals develops on a fast time scale. (We show in Table 10 that for relevant parameter values, $\epsilon_i \simeq 0.04 \ll 1$, so this limit is appropriate.) This quasi-stationary distribution is defined by the steady state equations:

$$0 = \frac{\partial^2 c_1}{\partial x^2} + a^2(m - c_1), \qquad 0 = \frac{\partial^2 c_2}{\partial x^2} + (m - c_2).$$

Solutions of these equations can be expressed in terms of the *Green's functions*:

$$c_1(x) = \frac{a}{2}\int_{-\infty}^{\infty} e^{-a|x-x'|}m(x')dx', \qquad c_2(x) = \tfrac{1}{2}\int_{-\infty}^{\infty} e^{-|x-x'|}m(x')dx'.$$

[This solution is valid on an infinite domain, but since the ratio of the chemical half-life time to the characteristic time for the chemical to diffuse over the domain length is small in our case, boundary conditions have little influence on the dynamics of the chemicals (Lee *et al.*, 2001).] These expressions indicate that at a point x, the chemical concentrations are linear superpositions of the concentrations resulting from secretions of each of the cells. A cell at a point x' induces chemical concentrations in its vicinity that decay exponentially with distance, $c_1 \sim \exp(-a|x-x'|)$, $c_2 \sim \exp(-|x-x'|)$.

Substituting these expressions for the chemical concentrations into equation (7), we find that the equation for cell density can be expressed as a self-consistent integro-partial differential equation:

$$\frac{\partial m}{\partial t} = \frac{\partial^2 m}{\partial x^2} - \frac{\partial}{\partial x}(vm), \tag{12}$$

where

$$v = \frac{A_2}{2}(K * m) = \frac{A_2}{2}\int_{-\infty}^{\infty} K(x-x')m(x')dx' \tag{13}$$

represents the **drift velocity** of the cells. The function $K(x)$ is the **interaction kernel** given by

$$K(x) = \text{sign}(-x)(Ae^{-a|x|} - e^{-|x|}). \tag{14}$$

The interaction kernel $K(x-x')$ represents the effect of a cell at x' on the motion of a cell at the point x. The first term in this kernel stems from the gradient of chemoattractant induced by a cell at x'; the factor A represents the relative strength of attraction. The second term describes the mutual repulsion of the cells due to the gradient of chemorepellent. Since the direction of drift changes when the cells exchange places, K is an odd function.

When chemicals diffuse on a much faster time scale than the motion of the cells, the single nonlocal diffusion-advection equation (12) for the cell density approximates the behavior of the chemotactic system. The cells undergo biased random movement with constant effective diffusion, and the effective drift velocity of a given cell is a linear superposition of the velocities imposed by all other cells. The interaction kernel $K(x)$ describes the rate of drift of a cell at x induced by another cell at the origin. Negative (positive) values of $K(x)$ correspond to movement toward (away from) the origin. The parameters A, a affect the shape of the kernel $K(x)$, as shown in Fig. 3.

In the analysis and simulations below, we treat the full model. However, we comment on the connection between the behavior of the full model and that of the approximate nonlocal representation.

6. LINEAR STABILITY ANALYSIS

We here analyze the stability and bifurcation behavior of the full model consisting of equations (7)–(9). The homogeneous steady state cell and chemical distribution of these equations is $m = 1$, $c_1 = 1$, $c_2 = 1$. Consider small perturbations of the steady state of the form:

$$m(x,t) = 1 + m' e^{\sigma t} e^{iqx}, \tag{15a}$$

$$c_i(x,t) = 1 + c_i' e^{\sigma t} e^{iqx}, \tag{15b}$$

where

- $q = n\pi/L$ is the *wavenumber* of the perturbation, and the positive integer n is the *mode*. ($2L/n$ is the wavelength of the corresponding pattern.)
- σ represents the linear growth rate ($\sigma > 0$) or decay rate ($\sigma < 0$) of the perturbations.
- m' and c_i' are the (initially small) amplitudes of the perturbations at $t = 0$.

Substituting equations (15a) and (15b) into equations (7)–(9), linearizing the system of equations and computing the determinant of its Jacobian matrix, we obtain the following cubic equation for the eigenvalues σ:

$$\sigma^3 + \alpha\sigma^2 + \beta\sigma + \gamma = 0, \tag{16}$$

where

$$\alpha = q^2 + \frac{1}{\epsilon_1}(a^2 + q^2) + \frac{1}{\epsilon_2}(1 + q^2), \tag{17a}$$

$$\begin{aligned}\beta = {} & \left[\frac{1}{\epsilon_1}(a^2 + q^2) + \frac{1}{\epsilon_2}(1 + q^2) + \frac{A_2}{\epsilon_2} - \frac{a^2 A_1}{\epsilon_1}\right] q^2 \\ & + \frac{1}{\epsilon_1 \epsilon_2}(1 + q^2)(a^2 + q^2),\end{aligned} \tag{17b}$$

$$\gamma = \frac{1}{\epsilon_1 \epsilon_2}[(a^2 + q^2)A_2 - (1 + q^2)a^2 A_1 + (1 + q^2)(a^2 + q^2)]q^2. \tag{17c}$$

Equation (16) represents the **dispersion relation** associated with the model. Instability in the system and the corresponding onset of the pattern formation by cells and chemicals correspond to the condition $\mathrm{Re}(\sigma) > 0$.

The cubic equation (16) has real coefficients. The equation thus has three roots, one of which is always real; two others can be either real or complex conjugate depending on the model parameters. In the absence of chemotactic interactions ($A_1 = A_2 = 0$), the roots of equation (16) are readily found to be $\sigma_1 = -q^2$, $\sigma_2 = -(a^2 + q^2)/\epsilon_1$, $\sigma_3 = -(1 + q^2)/\epsilon_2$, and are all real and negative, so that the homogeneous steady state is stable. In the appendix, we further show that if chemoattraction is absent ($A_1 = 0$), all roots have negative real parts, so that, again, no pattern formation can occur.

When chemoattractant strength increases, a break of stability occurs at some finite value of A_1. The character of the bifurcation depends on parameter values, with two distinct scenarios possible: (1) a real root becomes zero (while the other roots have negative real parts); or (2) one real root is negative while two complex conjugate roots have their real part become zero (a Hopf bifurcation). We analyze both possibilities in detail in the appendix and show that scenario (1) occurs when $\gamma = 0$, $\alpha\beta - \gamma > 0$; while scenario (2) occurs when $\gamma > 0$, $\alpha\beta - \gamma = 0$. Which bifurcation takes place first thus depends on whether the expression $\alpha\beta - \gamma$ or γ becomes zero first, while the other is positive. If scenario (2) occurs, we expect a Hopf bifurcation, so that a pattern periodic in both space and time would evolve, whereas, in scenario (1), no temporal periodicity takes place.

For values of the model parameters discussed later on in this paper, random motion of the cells is much slower than the chemical diffusion, so that $\epsilon_1, \epsilon_2 \ll 1$. For this case, it turns out (as shown in the appendix) that the bifurcation follows scenario (1). Indeed, in this limit, $\alpha \simeq (a^2 + q^2)/\epsilon_1 + (1 + q^2)/\epsilon_2$, $\beta \simeq (a^2 + q^2)(1 + q^2)/(\epsilon_1\epsilon_2) > 0$. Using perturbation arguments, the three roots of equation (16) can be approximated as $\sigma_1 \simeq -\gamma/\beta$, $\sigma_2 \simeq -(a^2 + q^2)/\epsilon_1$ and $\sigma_3 \simeq -(1 + q^2)/\epsilon_2$. For biological relevance of the results to the system we are interested in modeling, we concentrate mainly on bifurcation under scenario (1): when the chemoattractant strength increases, $\alpha > 0$ and $\beta > 0$, and one real root becomes positive as soon as the inequality $\gamma < 0$ is satisfied. We comment in more detail on the second possibility of the Hopf bifurcation, for general theoretical interest, in Section 11 and in the appendix.

Based on the discussion above, the relevant condition for instability obtained from the linear analysis is

$$\gamma < 0. \tag{18}$$

Substituting equation (17c) into (18) gives the **instability condition**

$$\frac{A}{q^2 + a^2} - \frac{1}{q^2 + 1} > \frac{1}{A_2}. \tag{19}$$

This concludes the linear stability analysis of the full model.

It is interesting to remark on the connection between the full model of equations (7)–(9) and the approximate model given by equation (12). Linearization of equation (12) and substitution of the perturbation in the form $m(x, t) = 1 + m' e^{\sigma t} e^{iqx}$ leads to the dispersion relation:

$$\sigma = -q^2 + q^2 A_2 \left(\frac{A}{q^2 + a^2} - \frac{1}{q^2 + 1} \right) \equiv -q^2 + q^2 A_2 f(q),$$

where we have defined $f(q)$ as the expression in the braces. Similar calculations appear in Lee *et al.* (2001) and Mogilner and Edelstein-Keshet (1995). The condition $\sigma > 0$ is easily seen to give the same linear stability result for the approximate nonlocal equation (12) as for the full model.

7. RESULTS OF THE LINEAR STABILITY ANALYSIS

At the onset of instability, the behavior of the system is determined by the left-hand side of the instability criterion (19), and in particular, by the **bifurcation function** $f(q)$. For simplicity, we study the closely related function

$$F(x) = \frac{A}{x+a^2} - \frac{1}{x+1}, \tag{20}$$

where $x = q^2$ [so that $F(x(q)) = F(q^2) = f(q)$], The wavenumber(s) that correspond to values of x that satisfy the condition $F(x) > 1/A_2$ determine the wavelength of the growing pattern-forming mode. Regions of high density of cells ('clusters') are here associated with the putative AD plaques.

The function F is parameterized by the dimensionless parameters, A and a. Our goal in this section is to understand the distinct stability behaviors that are obtained for different ranges of these parameters. We consider the properties of $F(x)$ in the 2D parameter space Aa. The following three properties are crucial for understanding how instability can occur:

1. $F(x) \to 0$ as $x \to \infty$.
2. $F(0) = \frac{A}{a^2} - 1$. $F(0) > 0$ when $a < \sqrt{A}$, and $F(0) < 0$ when $a > \sqrt{A}$.
3. When $A \neq 1$, F has a critical point $(F'(x) = 0)$ at

   $$x = x_c \equiv \frac{a^2 - \sqrt{A}}{\sqrt{A} - 1} \equiv q_c^2. \tag{21}$$

   The corresponding critical wavenumber q_c is defined as the square-root of the expression in (21). For $A < 1$, $a < A^{1/4}$, the critical point, x_c is a minimum of the function F. For $A > 1$, $a > A^{1/4}$, the critical point is a maximum of F. Otherwise, F is monotonic for positive x.

Using the above features of F, stability of the model is characterized for several parameter regimes. In Fig. 1, we show the Aa parameter plane, together with arcs of the curves, (i) $A = 1$, (ii) $a = 1$, (iii) $a = A^{1/2}$, and (iv) $a = A^{1/4}$. In Figs 2 and 3, we plot the related bifurcation function, $f(q)$, and interaction kernel corresponding to parameter values from distinct domains of the Aa parameter plane. Several cases can be distinguished, one for each of the domains bounded by the above curves. We list these eight individual regimes and describe the behavior within each one in the appendix. Here we summarize the distinct behaviors:

1. When the chemorepulsion is strong and short-ranged (Region 1: $A < 1, a > A^{1/2}$), the homogeneous steady state is stable.
2. When the chemoattraction is strong and long-ranged (Region 2: $A < 1$, $a < A^{1/2}$ and $A > 1$, $a < A^{1/4}$), the homogeneous steady state is unstable. The linear stability analysis indicates that at the onset of instability, a long wavelength mode ($q_c \simeq 0$) would grow. This means that cells from the whole domain start to aggregate into a single cluster, or a few irregularly

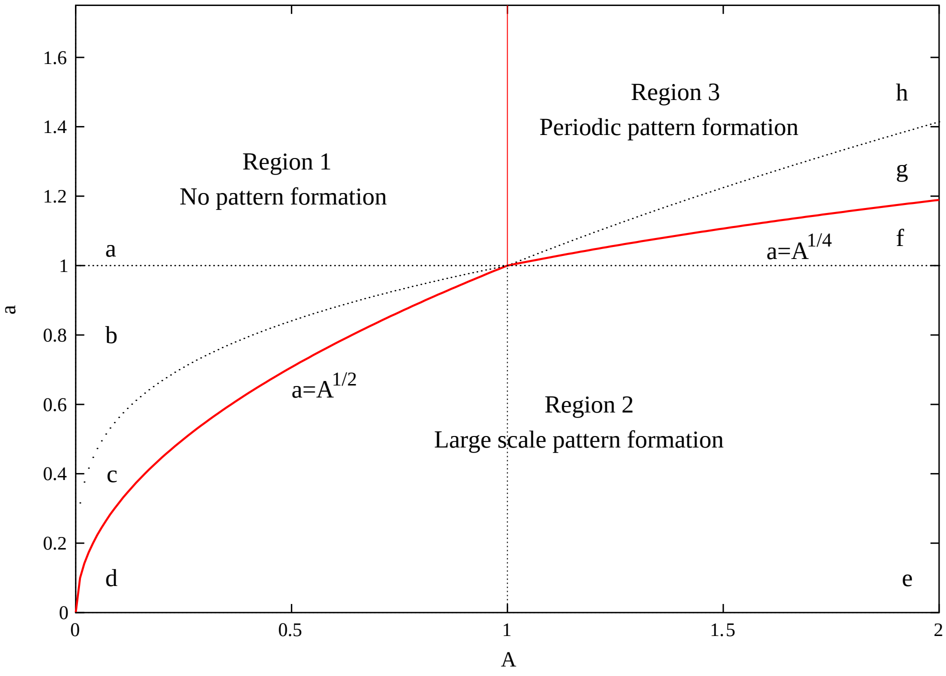

Figure 1. The parameter plane Aa, showing the curves (i) $A = 1$, (ii) $a = 1$, (iii) $a = A^{1/2}$, and (iv) $a = A^{1/4}$. Stability properties in each of the domains enclosed by these curves is described in the appendix and summarized in the text.

spaced clusters, the locations and sizes of which depend on initial conditions. Numerical simulations described in the next sections make these predictions more precise and detailed.

3. When there is a short-ranged chemoattraction and strong and long-ranged chemorepulsion (Region 3: $A > 1$, $a > A^{1/4}$), the homogeneous steady state is unstable. The linear stability analysis indicates that at the onset of instability, a periodic pattern with a finite wavelength would grow. Numerical simulations illustrate the sequence of events.
4. Using $A = (A_1/A_2)\,a^2$, it is informative to rewrite the instability criterion (19) in the form:

$$A_1 a^2 > k_1 A_2 + k_3. \tag{22}$$

Then $k_1 = [q^2 + a^2]/[q^2 + 1]$ and $k_3 = [q^2 + a^2]$ are constants of order 1 provided parameters are not too close to the boundaries of Region 3 in the Aa plane. This means that, in order for pattern formation to take place, the effect of chemotaxis should be stronger than the effect of random diffusion, and the strength of chemorepulsion should not greatly exceed that of chemoattraction. Furthermore, if the effective strength of attraction dominates repulsion too strongly, unstructured aggregation takes place. If attraction and repulsion have comparable strengths, but attraction has a

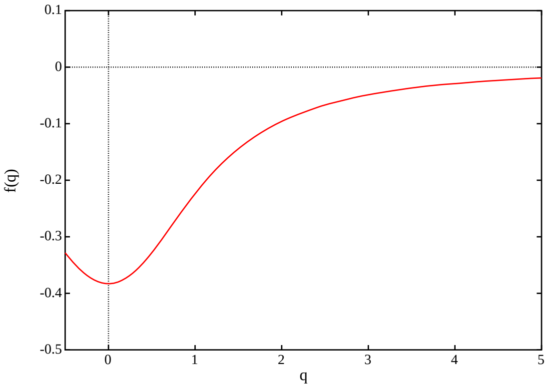

(a) Region 1b: $A = 0.5$, $a = 0.9$.

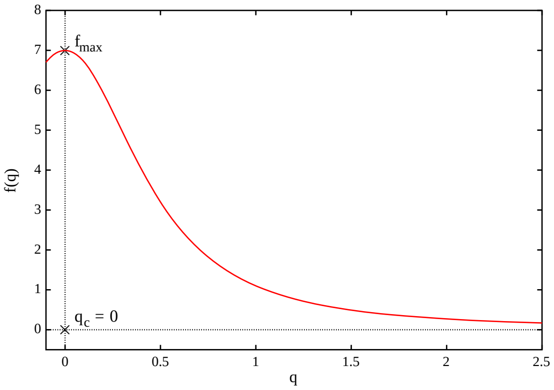

(b) Region 2e: $A = 2$, $a = 0.5$.

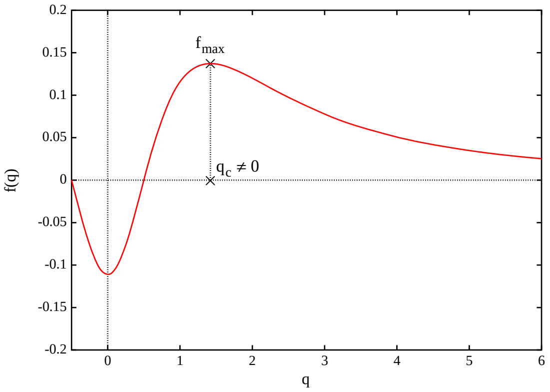

(c) Region 3h: $A = 2$, $a = 1.5$.

Figure 2. Shapes of the bifurcation function, $f(q)$ for parameter values in several regions of the Aa parameter plane. In case (a), $f(q) < 0$ implies that the uniform steady state is stable. In case (b), large scale instability is possible. In case (c), the function F has a maximum at a finite value that corresponds to a value of the wavenumber $q_c \approx 2$. This implies emergence of a periodic pattern when bifurcation occurs.

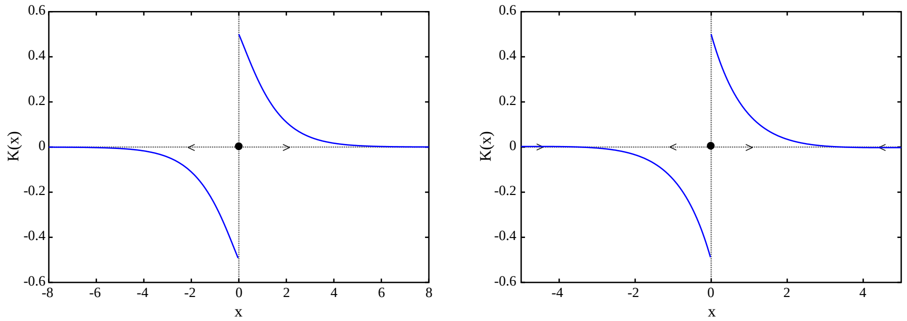

(a) Region 1a: $A = 0.5$, $a = 1.5$.

(b) Region 1b: $A = 0.5$, $a = 0.8$.

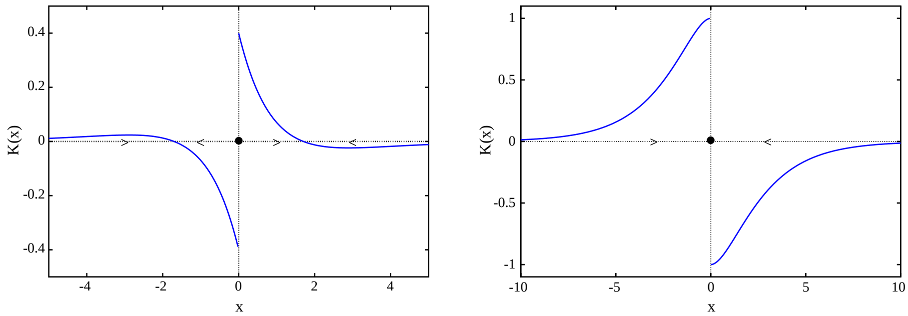

(c) Region 2d: $A = 0.6$, $a = 0.7$.

(d) Region 2e: $A = 2$, $a = 0.5$.

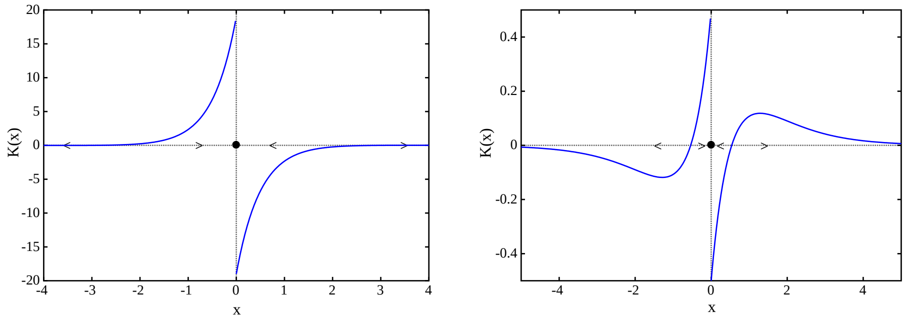

(e) Region 2e: $A = 2$, $a = 1.2$.

(f) Region 3: $A = 1.5$, $a = 1.75$.

Figure 3. Shapes of the interaction kernel $K(x)$ in the same regions of the parameter space Aa as in Fig. 2. This function represents the effect of a cell at the origin on the velocity of other cells at a distance x away from it. $K > 0$ ($K < 0$) corresponds to repulsion (attraction), or divergence (convergence) of the cells, as indicated by the arrows.

shorter range, $L_2 > k_3 L_1$, where $k_3 \sim 1$, then a pattern with an inherent scale evolves. The distance between the clusters of cells, determined by this inherent length scale, is of the same order as the range of the repulsion, L_2.

We illustrate the instability criterion given by equation (19) in Fig. 4. In this figure, all wavenumbers in the range between $q_{\min}$ and $q_{\max}$ would be unstable according to predictions of the linear stability theory. (The range of unstable wavenumbers can be seen to depend on $1/A_2$.) Below, we report the results of numerical simulations of the model equations for two sets of model parameters

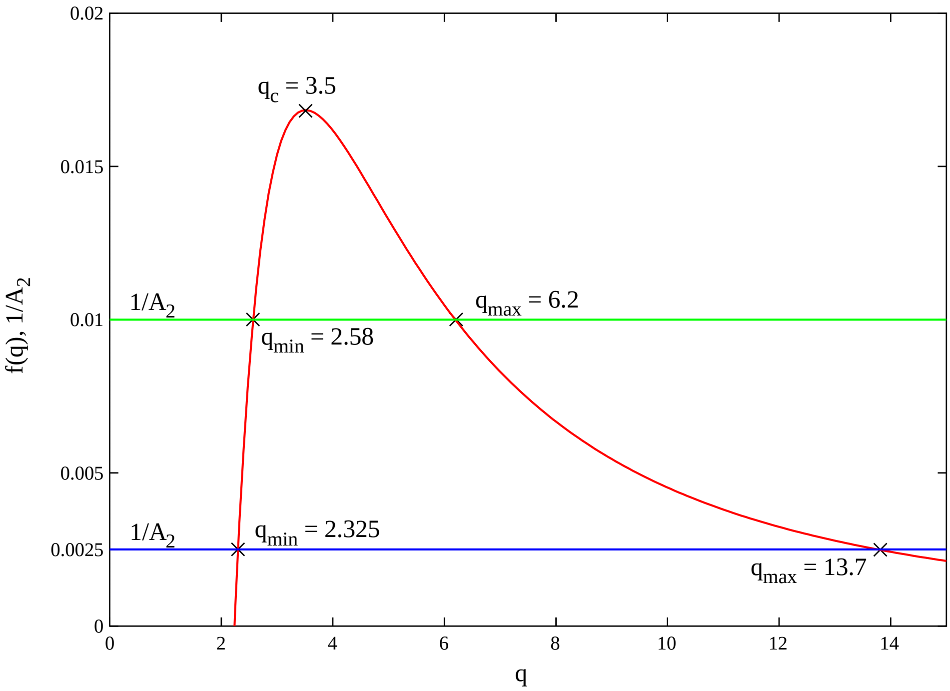

Figure 4. The bifurcation function $f(q)$ for $A = 1.5$, $a = 2$, and the line $y = 1/A_2$ for $A_2 = 100$ and 400. Values of q such that $f(q) > 1/A_2$ correspond to wavenumbers of the unstable modes.

from Region 3 in the *Aa* parameter space. (See Table 10 for the values of these parameters.) In each case, we plot the bifurcation function to find the range of the wavenumber q characterizing growing modes. For parameter Set 1 of Table 10, we find that modes $5 < n < 9$ grow. For parameter Set 2 of Table 10 (stronger chemotactic interactions), modes $4 < n < 21$ grow. For both sets of parameters, the most unstable mode is $n = 6$. The actual number of cell aggregates and characteristic distance between them cannot be derived from the linear stability analysis away from the bifurcation because of complex nonlinear interactions of the various growing modes. However, the number of peaks in the cell density that form inside the spatial domain correlates most closely with $q_{\max}$, the maximal unstable wavenumber. As the chemotactic interactions grow, $q_{\max}$ increases. Thus, stronger inter-cell interactions should lead to a greater number of more closely spaced aggregates, which we are interpreting in the model as AD plaques. Our numerical simulations below confirm this prediction.

8. PARAMETER ESTIMATES

In order to study the system numerically and compare predictions with biological data, we need to ascertain values of the model parameters. We use the following

Table 2. Calculated effective diffusion coefficients for cytokines and chemicals implicated in AD.

Molecule type	Value (μm^2/ min)	Reference
β-amyloid	1500	Goodhill (1997)
IL-1β	900	Goodhill (1997)
IL-6	810	Goodhill (1997), Moghe *et al.* (1995)
TNF-α	900	Goodhill (1997)

Table 3. Typical numbers of cytokine receptors per cell and calculated effective local receptor concentrations.

Cytokine	Receptors (r) per cell (macrophage)	Receptor concentration (r_c) (nM)	Source
IL-1β	5000	0.83	Benjamin *et al.* (1990)
IL-6	500	0.08	Yamaguchi *et al.* (1992)
TNF-α	4000	0.66	Michishita *et al.* (1990)

Table 4. Association rates (k_+), dissociation rates (k_-) and equilibrium constants (K_D) for cytokines to their receptors.

Cytokine	$[k_-]$ min^{-1}	$[k_+]$ nM^{-1} min^{-1}	$[K_D] = \frac{k_-}{k_+}$ nM	Source
IL-1β	0.004–0.04	0.004–0.04	1	Benjamin *et al.* (1990)
IL-6	0.047	0.012	4	Hammacher *et al.* (1996)
TNF-α	0.01	0.0036–0.05	0.2–2.8	Michishita *et al.* (1990) Pennica *et al.* (1992)

units for the model variables: min for time, μm for distance, nM for chemical concentrations and cells μm^{-3} for the density of cells. Refer to Tables 2–10 and calculations in the appendix for supporting material.

The diffusion coefficient of a molecule scales approximately as the $-1/3$ power of its molecular weight (Goodhill, 1997). The **effective diffusivity** of molecules such as soluble amyloid, cytokines IL-1β, IL-6, and TNF-α can be estimated using their known molecular weights (Table 2), leading to values for the parameters D_i. To correct for the fact that brain tissue is a heterogeneous, geometrically complex medium, we incorporated a correction factor of 50% to account for tortuosity of the neuronal extracellular space (Sykova, 1997; Mazel *et al.*, 1998; Nicholson and Sykova, 1998; Sykova *et al.*, 1998).

We assumed that the **rate of decay** of cytokines and amyloid was approximately the same as the rate of binding of these molecules to cell-surface receptors on neurons and other cells. The number of receptors on typical cells, and the dynamics

Table 5. Concentration of cytokines produced by microglia or astrocytes, in the presence of a stimulating factor. All values are from Lee *et al.* (1993). LPS = lipopolysaccharide.

Cytokine	Produced by	Value $\left(\frac{\text{pg}}{\text{ml}}\right)$	Comments (cells/ml)
IL-1β	Microglia (stimulated by LPS)	300	0.2×10^6 for 4 h
IL-6	Microglia (stimulated by LPS)	2000	0.2×10^6 for 4 h
TNF-α	Microglia (stimulated by LPS)	400	0.2×10^6 for 4 h
IL-6	Astrocytes (stimulated by IL-1β)	300	0.2×10^6 for 8 h
TNF-α	Astrocytes (stimulated by IL-1β)	80	0.2×10^6 for 8 h

Table 6. Production rates of cytokines produced by microglia or astrocytes, in the presence of a stimulating factor. All values were calculated using data from Lee *et al.* (1993). LPS = lipopolysaccharide.

Cytokine	Produced by / cell type	Value $\left(\frac{\text{pg}}{\text{min}}\right)$
IL-1β	Microglia (stimulated by LPS)	6.25×10^{-6}
IL-6	Microglia (stimulated by LPS)	41.67×10^{-6}
TNF-α	Microglia (stimulated by LPS)	8.33×10^{-6}
IL-6	Astrocyte (stimulated by IL-1β)	3.125×10^{-6}
TNF-α	Astrocyte (stimulated by IL-1β)	0.833×10^{-6}

of uptake of these receptors for the given cytokine is summarized in Tables 3 and 4 (Ding *et al.*, 1989; Benjamin *et al.*, 1990; Pennica *et al.*, 1992; Yamaguchi *et al.*, 1992). This led to estimates for the decay parameters b_i (Table 7 and calculations in the appendix). We assumed that if the tissue has average receptor concentration r_c (units of nM), and the association rate for cytokine to receptor is $k_+(\text{nM}^{-1}\ \text{min}^{-1})$, then the rate of removal of the chemical is on the order of $b \approx k_+ r_c$. Using the derived estimates for D_i and b_i, we could estimate the spatial ranges $L_i \approx \sqrt{D_i/b_i} = 300\ \mu$m: we found that the chemoattractant and chemorepellent spread over hundreds of microns before decay.

To estimate typical **rates of production** of cytokines IL-1β, IL-6, TNF-α, etc, we used experimental *in vitro* data for secretion of these factors (Lee *et al.*, 1993; Fiala *et al.*, 1998). Table 5 summarizes **concentration** of cytokines produced by

Table 7. Calculated decay rates of cytokines based on receptor binding as the rate limiting step in removal of the given chemical.

Cytokine	Absorbed by	Value (min^{-1})
IL-1β	Macrophage	0.003–0.03
IL-6	Macrophage	0.001
TNF-α	Macrophage	0.003–0.03

Table 8. Parameters characterizing movement of human neutrophils (Moghe *et al.*, 1995). These were used as estimates for microglia motion parameters.

Parameter	Description	Value
χ	Chemotaxis towards IL-8	6–780 $\frac{\mu\text{m}^2}{\text{nM}\cdot\text{min}}$
μ	Random motility	33 $\frac{\mu\text{m}^2}{\text{min}}$

a known number of microglia or astrocytes during a known fixed experimental time interval in the presence of a stimulating factor. Using these concentration values, we can derive approximate **production rates** and calculate the parameters a_i (Table 6 and the appendix).

The average densities of microglia vary by two orders of magnitude between healthy individuals and AD patients, as observed in postmortem brain sections (Itagaki *et al.*, 1989; Mackenzie *et al.*, 1995). Using the observed numbers of cells per known area or volume cited in these references, we estimated the average distance between the cells, and then computed an order of magnitude for the average cell density (Table 9). Knowing the rates of production and decay and the average cell density, we can estimate that the scale of chemical concentration varies in a range 0.01–1 μMs.

Chemotactic motion of microglia has been studied experimentally (Davis *et al.*, 1992; Nolte *et al.*, 1996), but the data is unsuitable for estimating the chemotactic coefficients. We use values estimated for other immune cells such as neutrophils and macrophages (Rivero *et al.*, 1989; Farrell *et al.*, 1990; Moghe *et al.*, 1995). The random motility coefficient μ was also corrected for tortuosity of the neuronal extracellular space through which these cells crawl. Knowing the value of μ, and previously estimated spatial ranges of the chemicals, we find that the time scale in the system, $\tau = L_2^2/\mu$, is close to 2 days. This estimate is quite sensitive to values of the parameters: should the spatial range be a few times smaller, the time scale would be on the order of a few hours.

Table 9 summarizes dimensional parameter values that appear in the chemo-attraction-repulsion equations (2) and (3). We select IL-1β as putative attractant and TNF-α as putative repellent for microglia, i.e., we identify c_1 = concentration of IL-1β and c_2 = concentration of TNF-α.

Table 9. Dimension-carrying parameter values used in the model.

Parameter	Description	Value	Comments
μ	Microglia random motility	$33\ \mu\text{m}^2\ \text{min}^{-1}$	Known value from Moghe *et al.* (1995)
χ_1	Chemoattraction	$6\text{–}780\ \frac{\mu\text{m}^2}{\text{nM}\cdot\text{min}}$	Known value from Moghe *et al.* (1995)
χ_2	Chemorepulsion	?	Not available
D_1	IL-1β diffusion	$900\ \mu\text{m}^2\ \text{min}^{-1}$	Calculated using Goodhill (1997)
D_2	TNF-α diffusion	$900\ \mu\text{m}^2\ \text{min}^{-1}$	Calculated using Goodhill (1997)
a_1	IL-1β production rate (per microglia cell)	$6.25 \times 10^{-6}\ \text{pg}\ \text{min}^{-1}$	Calculated using Lee *et al.* (1993)
a_2	TNF-α production rate (per microglia cell)	$8.33 \times 10^{-6}\ \text{pg}\ \text{min}^{-1}$	Calculated using Lee *et al.* (1993)
b_1	IL-1β decay rate	$0.003 - 0.03\ \text{min}^{-1}$	Calculated in this paper
b_2	TNF-α decay rate	$0.002\text{–}0.03\ \text{min}^{-1}$	Calculated in this paper
$\bar{m}$	Average cell density	$10^{-6} - 10^{-4}\text{cells}\ \mu\text{m}^{-3}$	Mackenzie *et al.* (1995), Itagaki *et al.* (1989)

Table 10. Dimensionless parameter values used in the numerical simulations.

Parameter	Set 1	Set 2	Set 3
A_1	37.50	150	37.14
A_2	100	400	27
ϵ_1	0.0367	0.0367	0.0367
ϵ_2	0.0367	0.0367	0.0367
a	2	2	1.1
A	1.5	1.5	1.7
Domain length	5	5	10

We calculated the dimensionless parameters A, a, A_i, ϵ_i, $i = 1, 2$ based on the above estimates for the model parameters, and found that $\epsilon_{1,2} \ll 1$, i.e., the chemicals diffuse much faster than the cells. Numerical experiments show that results are not very sensitive to these parameters. Since we have $D_1 = D_2$, it follows that $a > 1$ if $b_1 > b_2$, i.e., if IL-1β has a higher decay rate than TNF-α. Our estimates of the decay rates allow a wide range of values for the parameter a. In the numerical simulations, we chose values of a between 0.4 and 2.

It is hard to narrow down estimates for the parameters A_1, A_2 and A, since the chemoattraction parameter and cell density range over two orders of magnitude, while the chemorepulsion parameter χ_2 is not available at all. Using lower estimates for the chemoattraction parameter and cell density, we obtain the value $A_1 \sim 0.1$. On the other hand, with upper estimates of the model parameters, $A_1 \sim 100$ is four orders of magnitude greater.

The linear stability analysis and shapes of the bifurcation function at various values of parameters A_1, A_2 and a lead to the observation that when parameters A_1 and A_2 are much smaller than 1 (low cell densities and weak chemoattraction), then the homogeneous steady state is stable. However, when the cell density increases, as is known to occur in AD, and/or cells are more sensitive to secreted chemicals, A_1 can reach values of tens or hundreds, and then pattern formation is possible: see Fig. 4. The analysis of the previous section predicts that if repulsion is weak (the value of A_2 is too small), then unstructured aggregation takes place. On the other hand, if A_2 is too large, then there is no pattern formation at all. Thus, our theory predicts that stringent constraints on the strength of the chemorepulsion have to be satisfied in order for the evolution of discrete aggregates similar to observed senile plaques to evolve.

9. NUMERICAL SIMULATIONS

The numerical integration of chemotaxis equations is challenging because sharp peaks in the cell distribution tend to evolve. Previous researchers addressed these challenges in various ways. Finite element approximation using a Galerkin formulation was employed by Maini *et al.* (1991). Sherratt *et al.* (1992) used a semi-implicit finite difference scheme. In another case, the spatial derivatives of the PDEs were discretized using a uniform grid and centered differences so that the resulting ODEs were integrated with a stiff integrator package (Othmer and Stevens, 1997). (The authors noted, and we concur, that, in order to conserve particles, it is important to discretize the divergence form of the PDEs, rather than expand the derivative and then discretize the resulting equations.) When peaks began to grow, the time step was manually adapted to avoid numerical instability (Angela Stevens, personal communication).

We explored some simple fixed mesh techniques for solving our model equations numerically and found them unsuitable. Instead, we use an adaptive mesh technique (Huang *et al.*, 1994a,b). The main reason for using an adaptive mesh is to handle the sharp spikes that occur as aggregation sets in. Without spatial adaptivity, the narrowest structure that can be resolved is of the order of the *fixed* mesh separation. In the simulation, we have no *a priori* knowledge of when and where the aggregates form, excluding the usefulness of a fixed irregular grid. A fixed regular mesh would mean a prohibitive number of mesh points to resolve fine structures over the entire domain.

Adaptive mesh generation circumvents this problem by positioning mesh points in regions with high gradients. A monitor function is used to track some property of the solution, for example, arclength of the solution curve, to be distributed evenly between neighboring mesh points. Since our model involves several variables, we used the *sum* of the arclengths of the dependent variables as the monitor function. The mesh points are distributed by solving an auxiliary moving mesh PDE (Huang *et al.*, 1994a,b). This PDE is solved simultaneously with the model equations using a standard collocation technique for the spatial variable with variable time-stepping. For a review of the method see Huang *et al.* (1994a,b) and references therein.

We validated the code by comparing it with a fixed mesh and fixed time step method with several thousands of mesh points and a small time step. The latter had clear disadvantages compared to the moving mesh scheme, including incorrect predictions for locations and times of aggregate formation. For fixed mesh simulations, insufficient resolution also led to other spurious results such as overshoot, leading to negative cell and chemical concentrations close to edges of sharp peaks.

10. RESULTS OF THE NUMERICAL SIMULATIONS

We solved the model equations (7)–(9) numerically with the adaptive mesh method described above. In all numerical experiments, we used homogeneous initial distributions of the cells and chemicals with small superimposed random initial perturbations in the cell density and chemical concentrations. For values of A and a in Region 1 of the parameter space Aa ($A < 1$, $a > 1$, Fig. 1), the magnitudes of the initial perturbations decayed and asymptotically stable homogeneous cell and chemical densities evolved, in agreement with predictions of linear stability analysis.

Simulations in Region 2 of the parameter space Aa (Set 3 in Table 10) with a domain 10 spatial units wide, illustrate that long-ranged repulsion is not strong enough to keep the local cell aggregates separated (Fig. 5). Small initial random perturbations increase in amplitude and decrease in spatial frequency, so that a few mild cell peaks evolve, with shapes and locations determined by the random initial inhomogeneities. The small local aggregates of cells merge due to strong effective attraction, and after approximately 1 time unit, a few sharp peaks of density evolve. These local aggregates continue to drift toward each other and merge on a slower time scale. After a few time units, one very narrow and dense aggregate dominates the center of the spatial domain, while two others form at the boundaries. In some runs, all the peaks drifted toward the edges, and none remained inside the domain. Singular perturbation analysis (not reported in detail here) suggests that, after an exponentially large time, a single peak, whose location depends on initial conditions would remain. Clearly, this pattern formation scenario does not resemble the biological observations for Alzheimer's senile plaques.

Simulations from Region 3 of the parameter space Aa (given by the Sets 1 and 2 in Table 10) and a domain 5 spatial units wide are shown in Figs 6 and 7. The steady state nonhomogeneous densities evolved over roughly 1 time unit (corresponding to a few hours of real time). As in the previous case, a few mild peaks in the

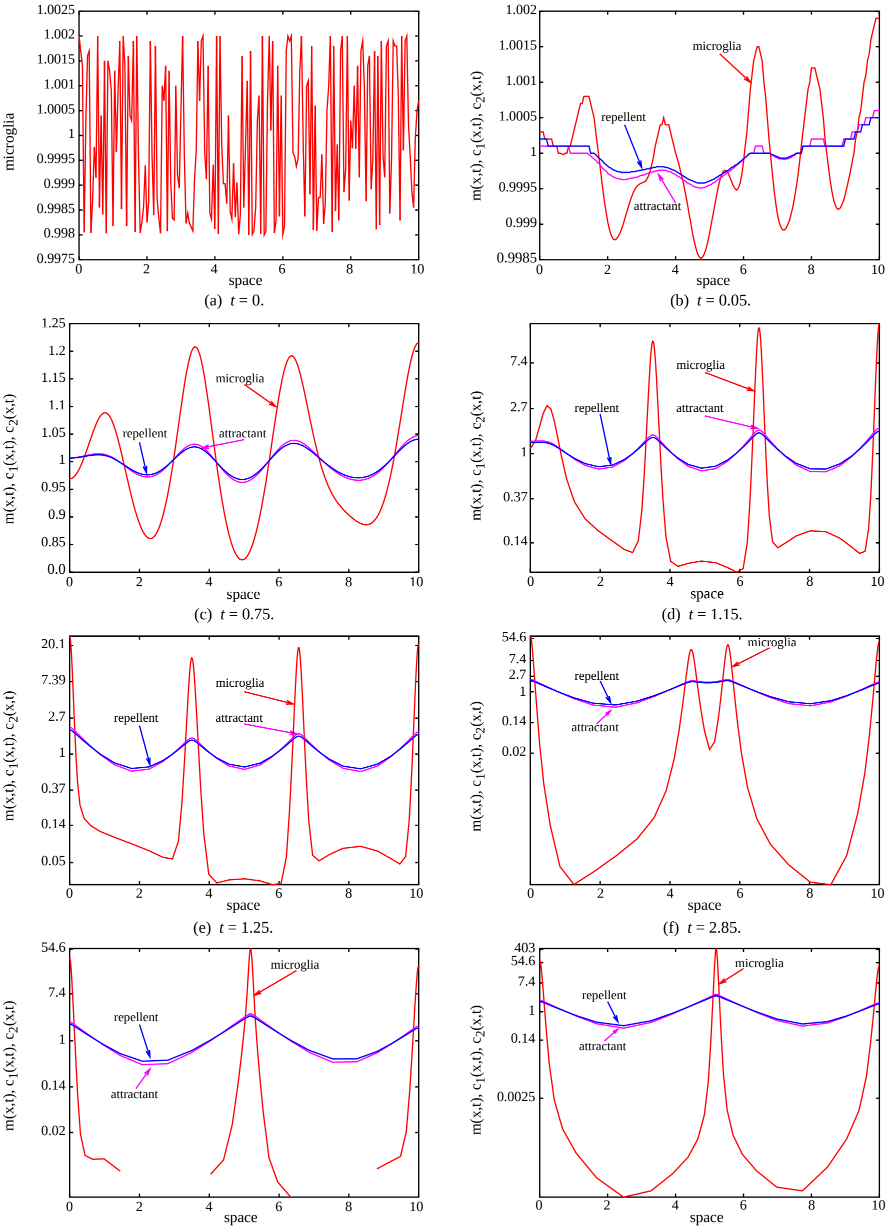

(a) $t = 0$.
(b) $t = 0.05$.
(c) $t = 0.75$.
(d) $t = 1.15$.
(e) $t = 1.25$.
(f) $t = 2.85$.
(g) $t = 2.9$.
(h) $t = 5.0$.

Figure 5. Numerical simulation for the evolution of spatial distributions of cells and chemicals using Set 3 parameter values (Table 10). Random initial conditions were used: $m(x, 0) = 1 + \epsilon x_{\text{ran}}$, $c_i(x, 0) = 1 + \epsilon x_{\text{ran}}$, $\epsilon = 0.002$, where x_{ran} is a uniform random variable, $|x_{\text{ran}}| < 1$. The vertical scale is logarithmic in parts (d), (e), (f), (g), (h). Three sharp peaks of the cell density evolve.

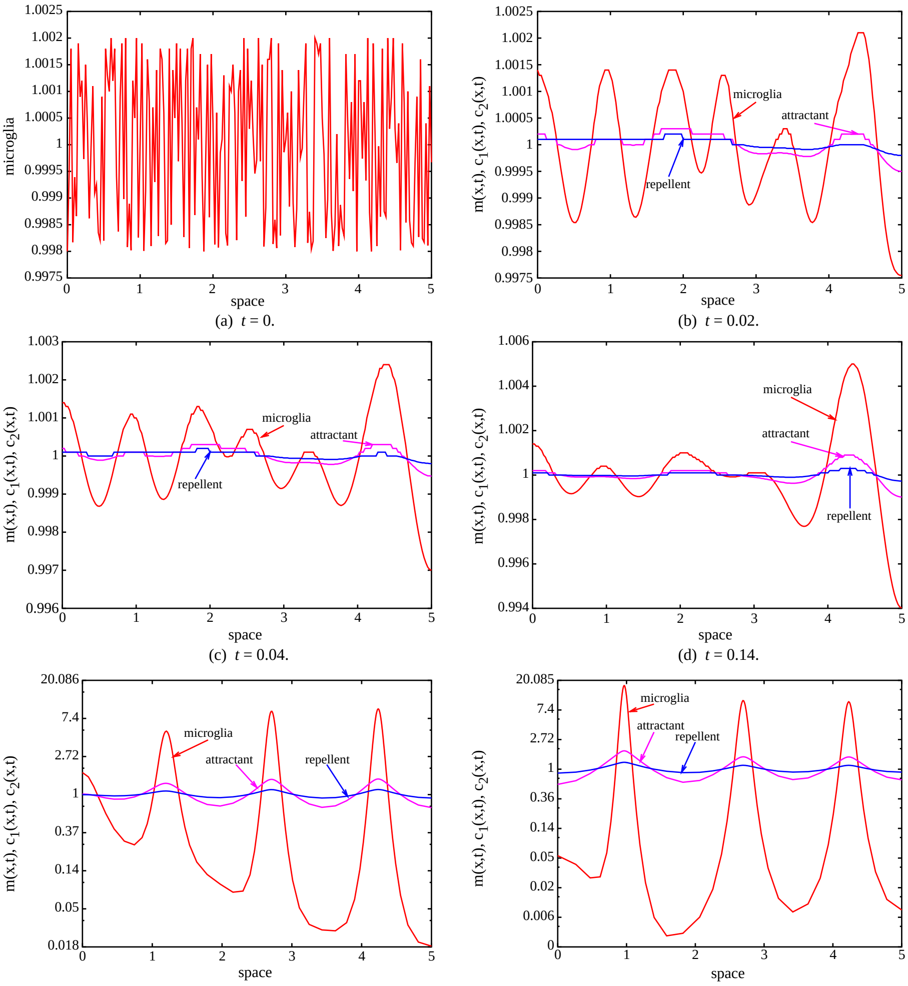

(a) $t = 0$. (b) $t = 0.02$.

(c) $t = 0.04$. (d) $t = 0.14$.

(e) $t = 1$. (f) $t = 2$.

Figure 6. Same as Fig. 5 but for parameter Set 1 (Table 10). The vertical scale is logarithmic in parts (e), (f). Three roughly equally spaced peaks of cell density evolve.

cell density evolve first. Due to strong long-ranged repulsion, these do not merge, but, rather, evolve into roughly equally spaced sharp peaks, in agreement with the stability analysis. For smaller values of A_1 and A_2 (weaker interactions or smaller cell density), three peaks evolved (see Fig. 6). For stronger interactions and/or greater density, six peaks evolved (see Fig. 7), also confirming the prediction of the stability analysis. The spatial period of the pattern that evolves is of order 1, in further agreement with the analysis.

11. OTHER PATTERN FORMATION SCENARIOS

As the chemoattraction–repulsion system has broader applicability to systems other than microglia and cytokines, we briefly comment on the theoretical case of

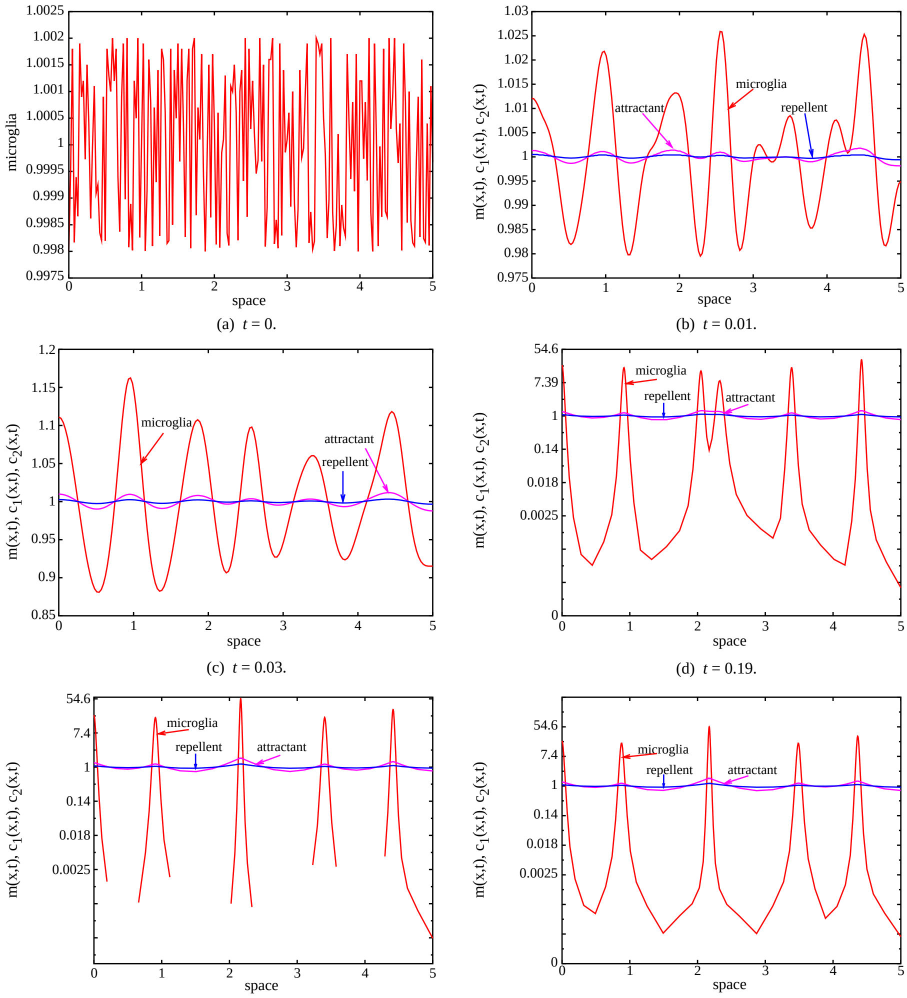

(a) $t = 0$.

(b) $t = 0.01$.

(c) $t = 0.03$.

(d) $t = 0.19$.

(e) $t = 0.2$.

(f) $t = 1$.

Figure 7. As in the previous two figures, but for the parameter Set 2 (Table 10). The vertical scale is logarithmic in parts (d), (e), (f). Six roughly equally spaced peaks of cell density evolve.

pattern formation that leads to periodicity in both space and time. This has been denoted ‘scenario (2)’ in our linear stability analysis, and is discussed in greater detail in the appendix.

We investigated the model numerically for one set of parameter values that lead to this scenario, namely, $\epsilon_1 = 2$, $\epsilon_2 = 10$, $a = 2$, $A_1 = 2$; $A_2 = 4$. Here, diffusion of the chemorepellent is much slower than that of the cells and the chemoattractant. The leading unstable mode is then characterized by the wavenumber $q_c \simeq 1$ and linear growth rate is $\sigma(q_c) \simeq 0.07 \pm 0.4i$, where $i = \sqrt{-1}$.

We solved the model system of equations with these parameter values. The results, shown in Fig. 8, confirm the linear stability prediction that standing waves

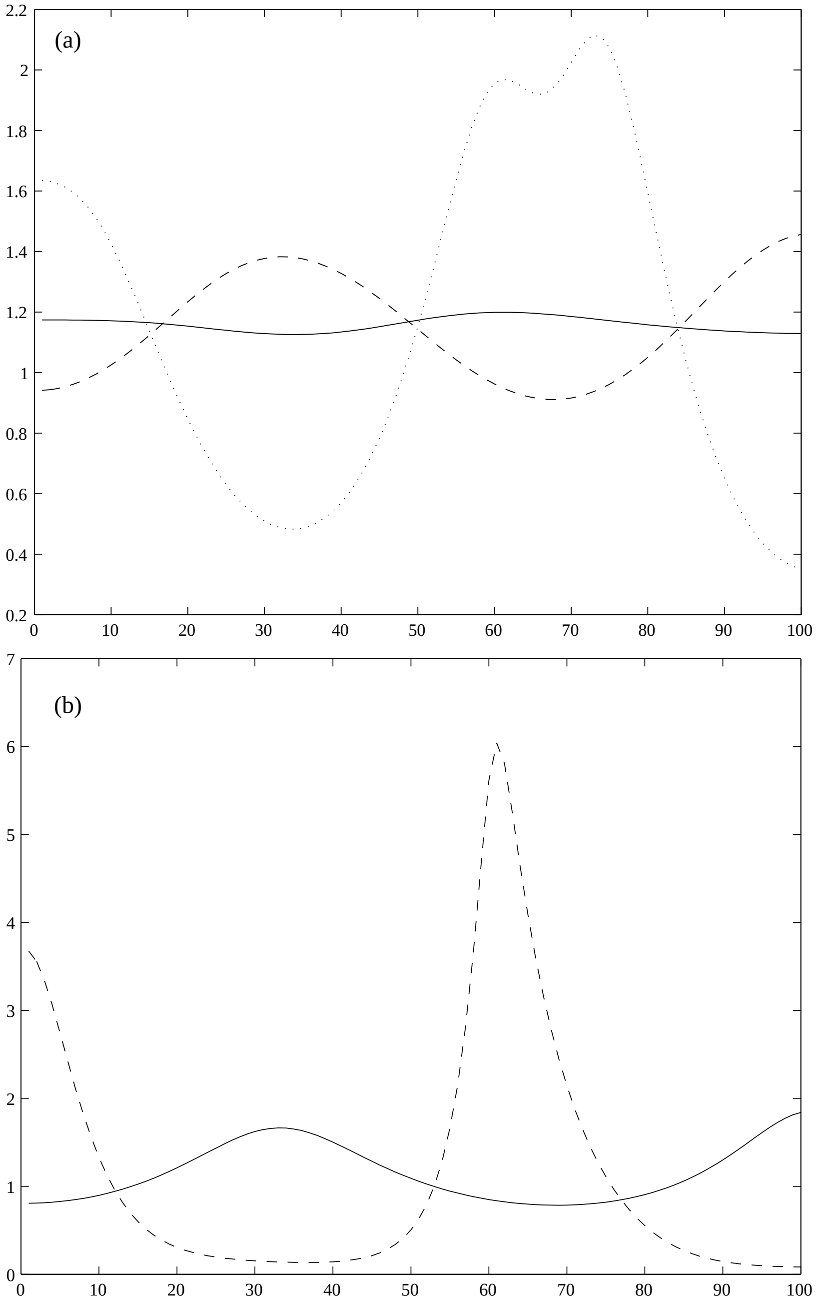

Figure 8. (a) Results of the numerical simulations of the model in the case of a Hopf bifurcation. A standing wave, periodic in space and time, evolves at the onset of the bifurcation. The solid, dashed, and dotted lines show profiles of the cell density (vertical axes) over space (horizontal axes) at $t = 15$, 23, and 30 time units, respectively. (b) Eventually, one or two sharp peaks in cell density evolve and the oscillations stop. The solid and dashed lines show the cell density profiles at $t = 25$ and 35 time units, respectively.

periodic in space and time will grow. However, experiments with many sets of parameter values (and no-flux boundary conditions) all lead to a similar result: a single peak of cell density eventually moves toward the closest edge of the 1D domain and stabilizes there. Simulated dynamics of the cells and chemicals can be viewed at `http://www.math.ucdavis.edu/~mogilner/PatForm.mov`. Initially, local aggregates of cells produce the diffusible attractant. This sets up local gradients promoting further cell aggregation. However, on a longer time scale, those cell aggregates produce local concentration of repellent. This eventually 'pushes' cells away, into the space between the aggregates, where repellent concentration and gradients are low. The cycle repeats, due to inherent delay between production, diffusion, and response to repellent. As a result, the cell (and attractant) density oscillates synchronously between maxima and minima at adjacent locations. However, in the end, the tendency to aggregate overcomes the influence of repulsion.

Though this phenomenon is of theoretical interest, it is unlikely to be relevant to plaques in AD, since these are not known to move or fluctuate periodically. A relevant observation in an unrelated system is that the rippling phenomenon in *Myxobacterial* colony sometime exhibits a standing wave pattern (Sager and Kaiser, 1994). Current theories explaining this phenomenon are based on contact interactions between cells [see Igoshin *et al*. (2001), and references therein]. However, the alternative mechanism of chemotactic interactions between the cells is not out of the question (Shi and Zusman, 1994).

12. DISCUSSION

Cells that secrete chemoattractants and chemorepellents will aggregate under chemotaxis, given appropriate conditions, as shown by our analysis and simulations. Chief among conditions for this to occur, are a sufficiently high cell density and a sufficiently sensitive chemotactic response. The type of aggregates that form depends on relative magnitudes and ranges of the attraction and repulsion. If repulsion is weak or short-ranged, then cells condense into a small number of large scale, unstructured aggregates whose locations are random; there is then no inherent spatial scale in the system. The most interesting situation occurs when both attraction and repulsion are strong: then provided attraction is short-ranged, while repulsion is long-ranged, periodic patterns will emerge, with dense cell aggregates distributed equidistantly. Numerical solutions demonstrate that cells are then highly concentrated at foci, with density decreasing sharply away from the aggregates. (Similarly, chemical concentrations are maximal at the foci and decay away slowly with distance from these aggregates.) This is fairly typical of AD plaque morphology (Itagaki *et al*., 1989).

Presently, the periodic formations of aggregates in the numerical simulations cannot be matched quantitatively with biological observations of the evolution of

Alzheimer's disease senile plaques. We can, however, compare the average spacing of theoretically predicted periodic structures with the experimental observations of those plaques. The model predicts that the spacing between clusters of microglia (i.e., between neighboring plaques) is on the order of the range of the chemorepellent, estimated in this paper to be a few hundred microns. This agrees with reported observations of inter-plaque distances in the range of 100 to several hundred μm (Itagaki *et al.*, 1989). When the average cell density grows, the characteristic spacing between cell aggregates should decrease. This prediction of the model is also in agreement with the observation of a positive correlation between the number of reactive microglia in the CNS and the number of plaques formed. Finally, to estimate the size of a plaque, we calculated the distance over which the microglia density decays by a factor of $1/e$ from its peak value [Figs 6(f) and 7(f)]. The simulation suggests plaque diameters in the range of 40–140 μm, close to the experimentally observed plaque sizes of 10–100 μm (Itagaki *et al.*, 1989).

Though the model described here was *motivated by* AD, it cannot be interpreted as evidence that chemotactic signaling of microglia are the single chief determinant of AD plaques: such (or alternate) conclusions must be based on biological experiments. At the same time, the model indicates that the parameter ranges relevant to underlying biological interactions of microglia do not rule out such a mechanism. The model has an independent scientific value in other biological systems in which chemoattraction and repulsion occur. Our main reason for testing its predictions in AD is that a relatively full set of parameters exists for the cell motions and chemical rates in this setting. However, before the validity of the model for AD can be accepted or dismissed, the following limitations have to be overcome. The roles of chemical attractants and repellents are suggested, but the evidence for their identity is circumstantial. More direct experimental evidence for the existence of such chemical interactions in the CNS is necessary. If our hypothesis for the nature of plaque formation is correct, better quantitative measurements of kinetic and motile parameters are needed. Careful statistical analysis of inter-plaque distances will have to be done in order to evaluate whether a dominant wavenumber indicating approximate periodicity exists. Further, numerical simulations should be expanded to 2D and 3D for comparison with experimental images [but see also, Edelstein-Keshet and Spiros (2002) for another approach with 2D simulations].

Even these barriers aside, the model has significant limitations. We neglected many relevant complex biological phenomena, including effects of developing plaques on neurons, and the feedbacks that result. The actual inflammatory process in AD consists of numerous cell types and chemical factors. We have represented one cell population (microglia), and auto-interaction chemicals that these cells produce (directly or indirectly), thus ignoring the much more complex actual network of interacting chemical signals. Here we explored only a simple quasi-linear model, in which all parameters were constant, whereas in reality, cell motility, secretion rates and decay rates of chemicals may be more complicated inter-dependent functions. Further, changes occurring in tissue properties through the course of the disease would affect these parameters, introducing more complicated temporal behavior. Finally, the significant heterogeneity of brain tissue is an obstacle to continuous models. Nevertheless, our model could be a useful theoretical tool complementing experimental research of AD.

It is not currently known precisely what governs the formation and locations of senile plaques in the brain. Other mechanisms might influence the distribution and relative spacing of those plaques. Some alternate mechanisms have been postulated. (1) Abnormally phosphorylated tau protein, which leads to incorrect microtubule assembly in neurons, results in neurofibrillary tangles, and can lead to eventual neuronal death (Rapoport *et al*., 2002). (2) Excitotoxic factors, and/or oxidative stress can similarly cause neuronal death. Those sites of dead and dying neurons could be the seeds around which plaques develop. If this were the case, then the aggregation of microglia at such sites would be a downstream effect, rather than a proximal cause in the initiation of the senile plaques. In that case, our chemotaxis-based model would not be appropriate as a description of the pathology.

Other mechanisms of pattern formation that have been investigated in mathematical biology so far are unlikely candidates for the development of plaques. First of all, Turing-like pattern formation (Turing, 1952) has rather specific restrictions on chemical reaction terms that are unlikely to occur in the brain. Further, pattern formation based on mechanochemical interactions (Murray, 1993) is equally unrealistic biologically in the adult brain. Nevertheless, at the present level of knowledge, we cannot rule out other mechanisms of pattern formation that could be responsible for plaques. Other systems involving one or more types of cells and various combinations of chemoattractants and/or chemorepellents could be further explored. For example, two attractants, one of which is *secreted homogeneously by the brain tissue and degraded by the motile cells* could be the case. In this paper, our goal was to investigate one of the simplest situations, which paves the road for more biologically realistic and mathematically thorough and exhaustive modeling.

ACKNOWLEDGEMENTS

ML, LEK, and ACR were supported by the Mathematics of Information Technology and Complex Systems (MITACS) under the Networks of Centers of Excellence program (Canada), and by a NSERC (Canada) research grant held by LEK. Derivation of parameter values was supported by In Silico Biosciences (R. Carr, President). AM is supported by a UCD Chancellor's fellowship, NSF Award DMS-0073828 and NIH GLUE grant 'Cell Migration Consortium' NIGMS U54 GM64346. The authors are grateful to Bob Russell (SFU) and Ricardo Carretero (SDSU) for making their adaptive mesh software available, and for their great help and advice in running the code.

APPENDIX

Linear stability and bifurcation analysis. In connection with equation (16), we first make the following general observations:

- The cubic equation (16) has real coefficients. The equation thus has three roots, one of which is always real; two others can be either real or complex conjugate depending on the model parameters.
- It is well known (and easily verified) that the coefficients are formed by $\alpha = -(\sigma_1 + \sigma_2 + \sigma_3)$, $\beta = \sigma_1\sigma_2 + \sigma_1\sigma_3 + \sigma_2\sigma_3$, and $\gamma = -\sigma_1\sigma_2\sigma_3$, where $\sigma_1, \sigma_2, \sigma_3$ are the three roots of (16).
- From the above item, it follows directly that if $\gamma > 0$ then either one or three of the roots have negative real parts, and if $\gamma = 0$, there is a zero root.
- The special case of one real root equal to zero and two other negative real roots ($\sigma_1 < 0, \sigma_2 < 0, \sigma_3 = 0$) implies $\alpha = -(\sigma_1 + \sigma_2) > 0$, $\beta = \sigma_1\sigma_2 > 0$, $\gamma = 0$. We characterize this with the pair of conditions $\gamma = 0$, $\alpha\beta - \gamma > 0$, and it corresponds to bifurcation scenario (1).
- The special case of one negative real root λ and two pure imaginary roots $\pm bi$ is found to satisfy $\alpha = \lambda > 0$, $\beta = b^2 > 0$, $\gamma = \alpha\beta = \lambda b^2$. We characterize this case, which leads to scenario (2), with the conditions $\gamma > 0$, $\alpha\beta - \gamma = 0$. Further the roots can be found exactly by factoring the cubic polynomial, i.e., $\sigma_1 = -\alpha$, $\sigma_{2,3} = \pm\sqrt{\beta}i$. (This scenario is the Hopf bifurcation.)
- From the above, we see that the expression $(\alpha\beta - \gamma)$ plays an important role in bifurcation. If all roots have negative real parts it is easy to show that $(\alpha\beta - \gamma) > 0$. Conversely, if $\gamma > 0$, and also $(\alpha\beta - \gamma) > 0$, then all three roots have negative real parts, a result that follows from continuity and the above arguments about bifurcation behavior.

Now, specifically in the case of the coefficients given by the expressions (17a)–(17c), we also conclude the following:

- If $A_1 = A_2 = 0$, the roots are real and negative: $\sigma_1 = -q^2$, $\sigma_2 = -(a^2 + q^2)/\epsilon_1$ and $\sigma_3 = -(1 + q^2)/\epsilon_2$. (This can be verified by substitution, or by noting the product and sum of the roots in coefficients γ and α.)
- α is always positive, while β and γ are decreasing functions of the chemoattractant parameter A_1.
- In the absence of chemoattraction ($A_1 = 0$), at arbitrary level of chemorepulsion, the expressions γ and $(\alpha\beta - \gamma)$ are positive.

The above assertions imply that when there is no chemoattraction, all three roots have negative real parts, so that no pattern formation can occur.

We now consider the two distinct bifurcation scenarios:

- (1) At some critical value of A_1, $\gamma = 0$, while $\beta > 0$. If this is the case, a *real* root of equation (16) is equal to zero. At greater values of A_1, this root becomes positive.

- (2) At a critical value of A_1, $\gamma > 0$ and $\beta > 0$, while $(\alpha\beta - \gamma) = 0$. If this is the case, a pair of *imaginary* conjugate roots of equation (16) exist. At greater values of A_1, these complex conjugate roots will have a positive real part. (This is a Hopf bifurcation.)
- Depending on the value of the other model parameters, as the parameter A_1 increases, either $\min_q(\gamma)$ becomes equal to zero first, before $\min_q(\alpha\beta - \gamma)$ is equal to zero (scenario 1), or the other way around (scenerio 2).
- In the limit $\epsilon_1, \epsilon_2 \ll 1$, when the chemoattractant strength increases, $\alpha > 0$ and $\beta > 0$, and one real root becomes positive as soon as the inequality $\gamma < 0$ is satisfied, i.e., the bifurcation follows the first scenario.

The case of the Hopf bifurcation and spatio-temporal pattern formation. We consider here pattern formation under scenario (2), when, at a critical chemoattractant strength $\gamma > 0$ and $\beta > 0$, while the function $(\alpha\beta - \gamma)$ changes sign from negative to positive. In that case, the real part of two complex conjugate roots changes sign from negative to positive.

- This is possible, for example, when *the chemorepellent diffusion is much slower than the diffusion of the cells and chemoattractant*, $(\epsilon_1 \sim 1, \epsilon_2 \ll 1)$. In that case, $(\alpha\beta - \gamma) \propto (a^2 + q^2) - a^2 A_1$, while $\gamma \propto (1 + q^2)[(a^2 + q^2) - a^2 A_1] + (a^2 + q^2)A_2$. This implies that the function $(\alpha\beta - \gamma)$ always becomes zero earlier than the function γ, as the parameter A_1 increases.
- Other cases are possible: for example, when $\epsilon_1, \epsilon_2 \ll 1$, while A_1, $A_2 \gg (1/\epsilon_{1,2})$, with certain additional restrictions on these parameters. Such cases could be biologically realistic. (Values of parameter Set 2 of Table 10, are close to, but not precisely in that region.) There is no simple analytical criteria for this type of bifurcation, but equation (16) can be easily solved numerically for a given parameter set, as discussed in Section 11.
- The leading mode in this case is characterized by a finite value of q. This can be seen from numerical solutions of equation (16), and from the following analytical argument: when $q \to 0$, $(\alpha\beta - \gamma) \to (a^2)(\epsilon_1 + a^2\epsilon_2)/(\epsilon_1^2\epsilon_2^2) > 0$.
- Numerical experiments discussed in the text were carried out for parameter values that lead to this scenario: $\epsilon_1 = 2$, $\epsilon_2 = 10$, $a = 2$, $A_1 = 2$; $A_2 = 4$. Then $\gamma > 0$ for all values of the wavenumber q, while $(\alpha\beta - \gamma)$ becomes negative at values of $q \simeq 1$. We numerically found roots of equation (16) using Matlab$^{\text{TM}}$. This also allowed us to determine the leading unstable wavenumber and linear growth rate.

Details of the Aa parameter plane regimes.

1. Region 1a $(A < 1, a > 1)$: The attraction has a weaker strength and smaller range than the repulsion. Therefore, the interaction kernel [Fig. 3(a)] is positive for $x > 0$ and cells always repel one another. The function F, and hence also the bifurcation function $f(q)$, is always negative so the

homogeneous steady state is stable at all wavenumbers, and there is no pattern formation.

2. Region 1b ($A < 1, A^{1/4} < a < 1$): Attraction has a smaller amplitude, but larger range than repulsion. The interaction kernel is positive for small distances $x > 0$, and negative further away [Fig. 3(b)]. Effectively, there is a strong short-ranged repulsion and a weak long-ranged attraction between cells. The bifurcation function is still negative at all values of the wavenumber [Fig. 2(a)]; the homogeneous steady state is stable.
3. Region 1c ($A < 1, A^{1/2} < a < A^{1/4}$): The situation is as in the previous case [Fig. 3(b)]. Here F has a critical point, but it is a minimum, and occurs for negative F. (This implies that the bifurcation function $f(q)$ is negative at the corresponding critical wavenumber.) There is no pattern formation.
4. Region 2d ($A < 1, a < A^{1/2}$): Qualitatively, the interaction kernel is the same as in the previous two cases. However, the long-ranged attraction is now strong enough [Fig. 3(c)] that the function F is positive at small values of x and has maximum $F(0) = ((A/a^2) - 1) > 0$ at $x = 0$ [Fig. 2(b)]. The most unstable mode is characterized by the smallest possible wavenumber $q = 0$. We therefore expect aggregation to develop on the scale of the whole spatial domain (Cross and Hohenberg, 1993).
5. Region 2e ($A > 1, a < 1$): In this region, both strength and range of attraction are greater than those of the repulsion, and the cells mutually attract at all distances [Fig. 3(d)]. The function F is positive at all values of x with a maximum at $x = 0$. The character of the instability is the same as in the previous case.
6. Region 2f ($A > 1, 1 < a < A^{1/4}$): Attraction has a larger magnitude but smaller range than repulsion; this is the case of short-ranged attraction and long-ranged repulsion [Fig. 3(e)]. However, the repulsion is so weak that the bifurcation function and the character of the instability are qualitatively the same as in the previous case.
7. Region 3g ($A < 1, A^{1/4} < a < A^{1/2}$): There is short-ranged attraction and long-ranged repulsion. The latter is now strong enough that the character of the function F changes qualitatively: it acquires a maximum, and is positive at a positive value of $x = x_c$ which corresponds to the wavenumber $q_c = \sqrt{(a^2 - \sqrt{A})/(\sqrt{A} - 1)}$. Thus, the most unstable mode is characterized by this finite wavenumber. We expect a **periodic pattern** to develop (Cross and Hohenberg, 1993).
8. Region 3h ($A < 1, a > A^{1/2}$): The situation is qualitatively the same as in the previous case [Figs 2(c) and 3(f)].

Effective diffusivity of molecules.

1. The diffusion coefficient of a molecule in cytoplasm scales approximately as one over the cubic root of its molecular weight (Goodhill, 1997).

2. A molecule with a molecular weight of Mwt = 0.5 kDa has diffusion coefficient $D \approx 10^{-6}$ cm^2 s^{-1} $= 6000\ \mu\text{m}^2\ \text{min}^{-1}$ (Goodhill, 1997).
3. IL-1β has a molecular weight of $\text{Mwt}_1 = 17$ kDa and its diffusion coefficient is given by:

$$D_1 \approx D\sqrt[3]{\text{Mwt}/\text{Mwt}_1} = D/\sqrt[3]{34} \approx 1800\ \mu\text{m}^2\ \text{min}^{-1}\,.$$

4. A correction factor of one half takes into account tissue tortuosity. The effective diffusion coefficients shown in Table 2 are estimated similarly.

Concentration of cell surface receptors. The receptor concentration, r_c (Table 3), was calculated as follows:

1. We use the value $V = 10^4\ \mu\text{m}^3$ as the volume of a cell.
2. Let r be the number of receptors per cell. Since we would like to find the receptor concentration in units of nM, we have to convert the number of receptors per volume to nM

$$\begin{aligned} r_c &= r \text{ receptors} \times \frac{1}{V}\left[\frac{1}{\mu\text{m}^3}\right] \times \frac{1}{6.02 \times 10^{23}\text{ receptors}}[\text{mole}] \\ &= \frac{r}{V}\left[\frac{1}{\mu\text{m}^3}\right] \times \frac{1}{6.02 \times 10^{23}}[M \times L] \times 10^{15}\left[\frac{\mu\text{m}^3}{L}\right] \times 10^9\left[\frac{\text{nM}}{\text{M}}\right] \\ &= \left(\frac{r}{V} \times 1.66\right)\ \text{nM}. \end{aligned}$$

3. For example, we find the receptor concentration of IL-1β to be

$$r_c = \frac{5 \times 10^3}{10^4} \times 1.66\ \text{nM} = 0.83\ \text{nM}.$$

Production rates of chemicals. We estimate the production rates of chemicals using the following calculations:

$$a_i = \text{amount}\left[\frac{\text{pg}}{\text{ml}}\right] \times \frac{1}{n\text{ cells}}[\text{ml}] \times \left[\frac{1}{\text{min}}\right]\ \text{per cell}.$$

For example, we find that one microglia cell secretes the following amount of IL-1β per minute:

$$\frac{300}{4 \times 60 \times 0.2 \times 10^6}\left[\frac{\text{pg}}{\text{min}}\right] = 6.25 \times 10^{-6}\left[\frac{\text{pg}}{\text{min}}\right].$$

The following conversion from the units of $\mathrm{pg}/\mu\mathrm{m}^3$ into the units of nM is used in order to express the production rates in the units of $\mathrm{nM} \times \mu\mathrm{m}^3/\,\mathrm{min}$:

$$\begin{aligned}
1\left[\frac{\mathrm{pg}}{\mu\mathrm{m}^3}\right] &= 1\left[\frac{\mathrm{pg}}{\mu\mathrm{m}^3}\right] \times 10^{15}\left[\frac{\mu\mathrm{m}^3}{L}\right] \times 10^{-15}\left[\frac{\mathrm{kg}}{\mathrm{pg}}\right] \times (6.02 \times 10^{23})\left[\frac{\mathrm{kDa}}{\mathrm{kg}}\right] \\
&\quad \times \frac{1\ \mathrm{molecule}}{\mathrm{Mwt}}\left[\frac{1}{\mathrm{kDa}}\right] \times \frac{1}{6.02 \times 10^{23}\mathrm{molecules}}[M \times L] \\
&\quad \times 10^{9}\left[\frac{\mathrm{nM}}{\mathrm{M}}\right] \\
&= \frac{10^9}{\mathrm{Mwt}}\ \mathrm{nM}.
\end{aligned}$$

Here Mwt is the molecular weight in kDa of either IL-1β or TNF-α.

REFERENCES

Alt, W. (1980). Biased random walk models for chemotaxis and related diffusion approximations. *J. Math. Biol.* **9**, 147–177.

Bagnard, D., N. Thomasset, M. Lohrum, A. W. Püschel and J. Bolz (2000). Spatial distributions of guidance molecules regulate chemorepulsion and chemoattraction of growth cones. *J. Neurosci.* **20**, 1030–1035.

Banati, R. B. and K. Beyreuther (1995). Alzheimer's disease, in *Neuroglia*, Chapter 68, H. Kettenmann and B. R. Ransom (Eds), New York: Oxford University Press, pp. 1027–1043.

Benjamin, D., S. Wormsley and S. Dower (1990). Heterogeneity in interleukin (IL)-1 receptors expressed on human B Cell lines. Differences in the molecular properties of IL-1 alpha and IL-1 beta binding sites. *J. Biol. Chem.* **265**, 9943–9951.

Benveniste, E. N. (1995). Cytokine production, in *Neuroglia*, Chapter 5, H. Kettenmann and B. R. Ransom (Eds), New York: Oxford University Press, pp. 700–713.

Chicoine, M. R., C. L. Madsen and D. L. Silbergeld (1995). Modification of human glioma locomotion in vitro by cytokines EGF, bFGF, PDGFbb, NGF and TNF-α. *Neurosurgery* **36**, 1165–1171.

Cowley, G. (2000). Alzheimer's: unlocking the mystery. *Newsweek* **January**, 46–51.

Cross, M. and P. Hohenberg (1993). Pattern formation outside of equilibrium. *Rev. Modern Phys.* **65**, 851–1112.

Davis, J. B., H. F. McMurray and D. Schubert (1992). The amyloid beta-protein of Alzheimer's disease is chemotactic for mononuclear phagocytes. *Biochem. Biophys. Res. Commun.* **189**, 1096–1100.

Davis, J. N. and J. C. Chisholm (1997). The 'amyloid cascade hypothesis' of AD: decoy or real McCoy? *Trends Neurosci.* **20**, 558–559.

de Castro, F., L. Hu, H. Drabkin, C. Sotelo and A. Chédotal (1999). Chemoattraction and chemorepulsion of olfactory bulb axon by different secreted semaphorins. *J. Neurosci.* **19**, 4428–4436.

Dickson, D. W. (1997). The pathogenesis of senile plaques. *J. Neuropathol. Exp. Neurol.* **56**, 321–339.

Ding, A., E. Sanchez, S. Srimal and C. Nathan (1989). Macrophages rapidly internalize their tumor necrosis factor receptors in response to bacterial lipopolysaccharide. *J. Biol. Chem.* **264**, 3924–3929.

Edelstein-Keshet, L. and A. Spiros (2002). Exploring the formation of Alzheimer's disease senile plaques in silico. *J. Theor. Biol.* **216**, 301–326.

Farrell, B., R. Daniele and D. Lauffenburger (1990). Quantitative relationships between single-cell and cell-population model parameters for chemosensory migration responses of alveolar macrophages to C5a. *Cell Motil. Cytoskeleton* **16**, 279–293.

Fiala, M. *et al.* (1998). Amyloid-β induces chemokine secretion and monocyte migration across a human blood-brain barrier model. *Mol. Med.* **4**, 480–489.

Goodhill, G. J. (1997). Diffusion in axon guidance. *Eur. J. Neurosci.* **9**, 1414–1421.

Grindrod, P., J. Murray and S. Sinha (1989). Steady-state spatial patterns in a cell-chemotaxis model. *IMA J. Math. Appl. Med. Biol.* **6**, 69–79.

Grunbaum, D. (1994). Translating stochastic density-dependent individual behavior to a continuum model of animal swarming. *J. Math. Biol.* **33**, 139–161.

Grunbaum, D. (1999). Advection-diffusion equations for generalized tactic searching behaviors. *J. Math. Biol.* **38**, 169–194.

Hammacher, A., R. Simpson and E. Nice (1996). The interleukin-6 (IL-6) partial antagonist (Q159E, T162P)IL-6 interacts with the IL-6 receptor and gp130 but fails to induce a stable hexameric receptor complex. *J. Biol. Chem.* **271**, 5464–5473.

Hardy, J. (1997). Amyloid, the presenilins and Alzheimer's disease. *Trends Neurosci.* **20**, 154–159.

Hillen, T. and A. Stevens (2000). Hyperbolic models for chemotaxis in 1D. *Nonlinear Anal. Real World Appl.* **1**, 409–433.

Huang, W., Y. Ren and R. Russell (1994a). Moving mesh methods based upon moving mesh partial differential equations. *J. Comput. Phys.* **113**, 279–290.

Huang, W., Y. Ren and R. Russell (1994b). Moving mesh partial differential equations (mmpdes) based on the equidistribution principle. *SIAM J. Numer. Anal.* **31**, 709–730.

Igoshin, O., A. Mogilner, R. Welsch, D. Kaiser and G. Oster (2001). Pattern formation and traveling waves in myxobacteria: theory and modeling. *Proc. Natl Acad. Sci. USA* **98**, 14913–14918.

Itagaki, S., P. L. McGeer, H. Akiyama, S. Zhu and D. Selkoe (1989). Relationship of microglia and astrocytes to amyloid deposits of Alzheimer's disease. *J. Neuroimmunol.* **24**, 173–182.

Jones, N. (2000). Soothing the inflamed brain. *Sci. Am.* **June**, 11–12.

Keller, E. F. and L. A. Segel (1970). Initiation of slime-mold aggregation viewed as an instability. *J. Theor. Biol.* **26**, 399–415.

Kowall, N. W. (1994). Beta amyloid neurotoxicity and neuronal degeneration in Alzheimer's disease. *Neurobiol. Aging* **15**, 257–258.

Lauffenburger, D. A. and C. Kennedy (1983). Localized bacterial infection in a distributed model for tissue inflammation. *J. Math. Biol.* **16**, 141–163.

Lee, C., M. Hoopes, J. Diehl, W. Gilliland, G. Huxel, E. v. Leaver, K. McCann, J. Umbanhowar and A. Mogilner (2001). Non-local concepts and models in biology. *J. Theor. Biol.* **210**, 201–219.

Lee, S., W. Liu, D. Dickson, C. Brosnan and J. Berman (1993). Cytokine production by human fetal microglia and astrocytes. Differential induction by lipopolysaccharide and IL-1. *J. Immunol.* **150**, 2659–2667.

Mackenzie, I. R., C. Hao and D. G. Munoz (1995). Role of microglia in senile plaque formation. *Neurobiol. Aging* **16**, 797–804.

Maini, P., M. Myerscough, K. H. Winters and J. Murray (1991). Bifurcating spatially heterogeneous solutions in a chemotaxis model for biological pattern generation. *Bull. Math. Biol.* **53**, 701–719.

Mark, M. D., M. Lohrum and A. W. Püschel (1997). Patterning neuronal connections by chemorepulsion: the semaphorins. *Cell Tissue Res.* **290**, 299–306.

Mazel, T., Z. Simonova and E. Sykova (1998). Diffusion heterogeneity and anisotropy in rat hippocampus. *NeuroReport* **9**, 1299–1304.

McLean, C., R. Cherny, F. Fraser, S. Fuller, M. Smith, K. Beyreuther, A. Bush and C. Masters (1999). Soluble pool of β-amyloid as a determinant of severity of neurodegeneration in Alzheimer's disease. *Ann. Neurobiol.* **46**, 860–866.

Michishita, M., Y. Yoshida, H. Uchino and K. Nagata (1990). Induction of tumor necrosis factor-α and its receptors during differentiation in myeloid leukemic cells along the monocytic pathway. a possible regulatory mechanism for TNF-α production. *J. Biol. Chem.* **265**, 8751–8759.

Moghe, P. V., R. D. Nelson and R. T. Tranquillo (1995). Cytokine-stimulated chemotaxis of human neutrophils in a 3-D conjoined fibrin gel assay. *J. Immunol. Methods* **180**, 193–211.

Mogilner, A. and L. Edelstein-Keshet (1995). Selecting a common direction: I. how orientational order can arise from simple contact responses between interacting cells. *J. Math. Biol.* **33**, 619–660.

Mrak, R. E., J. G. Sheng and W. S. Griffin (2000). Glial cytokines in neurodegenerative conditions, in *Neuro-Immune Interactions in Neurologic and Psychiatric Disorders*, Patterson, Kordon and Christen (Eds), Berlin: Springer, pp. 9–17.

Mrak, R. E., J. G. Sheng and W. S. T. Griffin (1995). Glial cytokines in Alzheimer's disease: review and pathogenic implications. *Human Pathology* **26**, 816–823.

Murray, J. D. (1993). *Mathematical Biology*, 2nd edn, Berlin, Heilderberg: Springer.

Myerscough, M., P. Maini and K. Painter (1998). Pattern formation in a generalized chemotactic model. *Bull. Math. Biol.* **60**, 1–26.

Nash, J. M. (2000). The new science of Alzheimer's. *Time* **July**, 32–39.

Nicholson, C. and E. Sykova (1998). Extracellular space structure revealed by diffusion analysis. *Trends Neurosci.* **21**, 207–215.

Nilsson, L., J. Rogers and H. Potter (1998). The essential role of inflammation and induced gene expression in the pathogenic pathway of Alzheimer's disease. *Front. Biosci.* **3**, 436–446.

Nolte, C., T. Moller, T. Walter and H. Kettenmann (1996). Complement 5a controls motility of murine microglial cells in vitro via activation of an inhibitory G-protein and the rearrangement of the actin cytoskeleton. *Neurosci. Sci.* **73**, 1109–1120.

Othmer, H. G., S. R. Dunbar and W. Alt (1988). Models of dispersal in biological systems. *J. Math. Biol.* **26**, 263–298.

Othmer, H. G. and A. Stevens (1997). Aggregation, blowup, and collapse: the ABC's of taxis in reinforced random walks. *SIAM J. Appl. Math.* **57**, 1044–1081.

Painter, K., P. Maini and H. Othmer (1999). Stripe formation in juvenile *pomacanthus* explained by a generalized Turing mechanism with chemotaxis. *Proc. Natl Acad. Sci. USA* **96**, 5549–5554.

Painter, K., P. Maini and H. Othmer (2000). Development and applications of a model for cellular response to multiple chemotactic cues. *J. Math. Biol.* **41**, 285–314.

Pennica, D., V. Lam, N. Mize, R. Weber, M. Lewis, B. Fendly, M. Lipari and D. Goeddel (1992). Biochemical properties of the 75-kDa tumor necrosis factor receptor. Characterization of ligand binding, internalization, and receptor phosphorylation. *J. Biol. Chem.* **267**, 21172–21178.

Rapoport, M., H. N. Dawes, L. I. Binder, M. P. Vitek and A. Ferriera (2002). Tau is essential to β-amyloid induced neurotoxicity. *PNAS* **99**, 6364–6369.

Rivero, M. A., R. T. Tranquillo, H. M. Buettner and D. A. Lauffenburger (1989). Transport models for chemotactic cell populations based on individual cell behavior. *Chem. Engineering Sci.* **44**, 2881–2897.

Sager, B. and D. Kaiser (1994). Intercellular c-signalling and the travelling waves of myxococcus. *Genes Development* **8**, 2793–2804.

Schaaf, R. (1985). Stationary solutions of chemotaxis systems. *Trans. Am. Math. Soc.* **292**, 531–556.

Selkoe, D. J. (1991). Amyloid protein and Alzheimer's disease. *Sci. Am.* **265**, 68–78.

Sheng, J. G., X. Q. Zhou, R. E. Mrak and W. S. T. Griffin (1998). Progressive neuronal injury associated with amyloid plaque formation in alzheimer disease. *J. Neuropathol. Exp. Neurol.* **57**, 714–717.

Sherratt, J. (1994). Chemotaxis and chemokinesis in eukaryotic cells: the Keller-Segel approximation to a detailed model. *Bull. Math. Biol.* **56**, 129–146.

Sherratt, J., E. Sage and J. Murray (1992). Chemical control of eukaryotic cell movement: a new model. *J. Theor. Biol.* **162**, 23–40.

Shi, W. and D. R. Zusman (1994). Sensory adaptation during negative chemotaxis in *Myxococcus xanthus*. *J. Bacteriol.* **176**, 1517–1520.

Smits, H., L. A. Boven, C. Pereira, J. Verhoef and H. S. L. M. Nottet (2000). Role of macrophage activation in the pathogenesis of Alzheimer's disease and human immunodeficiency virus type I-associated dementia. *Eur. J. Clin. Invest.* **30**, 526–535.

Stalder, M., A. Phinney, A. Probst, B. Sommer, M. Staufenbiel and M. Jucker (1999). Association of microglia with amyloid plaques in brains of APP23 transgenic mice. *Am. J. Pathol.* **154**, 1673–1684.

Streit, W. J. (1995). Microglia cells, in *Neuroglia*, Chapter 5, H. Kettenmann and B. R. Ransom (Eds), New York: Oxford University Press, pp. 85–96.

Sykova, E. (1997). The extracellular space in the CNS: Its regulation, volume, and geometry in normal and pathological neuronal function. *The Neuroscientist* **3**, 28–41.

Sykova, E., T. Mazel and Z. Simonova (1998). Diffusion constraints and neuron-glia interaction during aging. *Exp. Gerontol.* **33**, 837–851.

Tranquillo, R., S. Zigmond and D. Lauffenburger (1988). Measurement of the chemotaxis coefficient for human neutrophils in the under-agarose migration assay. *Cell Motil. Cytoskeleton* **11**, 1–15.

Turing, A. M. (1952). The chemical basis of morphogenesis. *Phil. Trans. R. Soc.* **B237**, 37–72.

Venters, H. D., R. Dantzer and K. W. Kelley (2000). A new concept in neurodegeneration: TNF-α is a silencer of survival signals. *Trends Neurosci.* **23**, 175–180.

Yamaguchi, M., M. Michishita, K. Hirayoshi, K. Yasukawa, M. Okuma and K. Nagata (1992). Down-regulation of interleukin 6 receptors of mouse myelomonocytic leukemic cells by leukemia inhibitory factor. *J. Biol. Chem.* **267**, 22035–22042.

Yao, J., L. Harvath, D. L. Gilbert and C. A. Colton (1990). Chemotaxis by a CNS macrophage, the microglia. *J. Neurosci. Res.* **27**, 36–42.

Received 19 July 2002 and accepted 25 February 2003